SANDIA REPORT

SAND2012-8414
Unlimited Release
Printed October 2012

Integration of Block-Copolymer with Nano-Imprint Lithography: Pushing the Boundaries of Emerging Nano-Patterning Technology

D. Bruce Burckel, C.-Y. Peter Yang, Elaine L. Yang, Charles A. Steinhaus, and Geoff L. Brennecka

Prepared by
Sandia National Laboratories
Albuquerque, New Mexico 87185 and Livermore, California 94550

Sandia National Laboratories is a multi-program laboratory managed and operated by Sandia Corporation, a wholly owned subsidiary of Lockheed Martin Corporation, for the U.S. Department of Energy's National Nuclear Security Administration under contract DE-AC04-94AL85000.

Issued by Sandia National Laboratories, operated for the United States Department of Energy by Sandia Corporation.

Available to DOE and DOE contractors from
U.S. Department of Energy
Office of Scientific and Technical Information
P.O. Box 62
Oak Ridge, TN 37831

Telephone: (865) 576-8401
Facsimile: (865) 576-5728
E-Mail: reports@adonis.osti.gov
Online ordering: http://www.osti.gov/bridge

Available to the public from
U.S. Department of Commerce
National Technical Information Service
5285 Port Royal Rd.
Springfield, VA 22161

Telephone: (800) 553-6847
Facsimile: (703) 605-6900
E-Mail: orders@ntis.fedworld.gov
Online order: http://www.ntis.gov/help/ordermethods.asp?loc=7-4-0#online

SAND2012-8414
Unlimited Release
Printed October 2012

Integration of Block-Copolymer with Nano-Imprint Lithography: Pushing the Boundaries of Emerging Nano-Patterning Technology

D. Bruce Burckel
Applied Photonic Microsystems Department

Geoff L. Brennecka
Electronic and Nanostructured Materials Department

Sandia National Laboratories
P.O. Box 5800
Albuquerque, New Mexico 87185-1411

C.-Y. Peter Yang
Weapons Subsystems 2 Department

Elaine L. Yang
ICMB Fuze Systems Engineering Department

Charles A. Steinhaus
Materials Physics Department

Sandia National Laboratories
P.O. Box 969
Livermore, California 94551-0969

ABSTRACT

The extreme nanoscale features prescribed by the International Technology Roadmap for Semiconductors (ITRS, *e.g.*, 11nm half-pitch for dense patterns and 4.5nm critical dimensions by 2022) require infrastructure-heavy extreme ultraviolet (EUV) and/or

alternative lithography approaches. We report here our efforts to direct the self-assembly of block copolymers (BCP) into device-oriented patterns initially defined by optical interference lithography (IL), and the use of self-assembled BCP patterns as masks to create nanoimprint lithography (NIL) masters via plasma etching. This project reported the first self-assembly of regular sub-20nm features directed by large-area patterns defined by interference lithography with up to 4x density multiplication. Simulation coupled with experimental verification explored critical parameters driving the complex three-dimensional configurations arising from surface interactions during directed self-assembly. NIL of BCP-defined features and patterns was demonstrated as a route to simple plasmonic structures with enhanced optical response. Finally, a non-destructive metrology framework was developed and demonstrated.

ACKNOWLEDGMENTS

As part of the National Institute for NanoEngineering, this work could not have even been conceived without significant contributions from and collaborations with university partners. The professors (and students) involved with this project were Paul Nealey (Charlie Liu, Lance Williamson) and Juan de Pablo (Darin Pike, Brandon Peters) from the University of Wisconsin and Steve Brueck (Alex Raub, Philip Hakeem, Ruichao Zhu) from the University of New Mexico. Two additional individuals who contributed quite heavily to this work but who left Sandia before completion of the project are Matt George (post-doc in 1816 during part of the project; left Sandia for a job at Moxtek) and Jack Skinner (staff member in 8226 during much of the project; left Sandia for a professorship at Montana Tech). Without Matt's guidance and perseverance in particular, significantly less would have been accomplished on this project. The authors would like to thank Chip Steinhaus and Mia Blea for their general technical assistance with a variety of aspects of this work. Bonnie McKenzie and Dick Grant both provided invaluable assistance in imaging of the samples. Finally, while neither was involved once the project was actually funded and underway, Alec Talin and Kate Bogart were instrumental in the initial development of the concepts and collaborations of this project.

CONTENTS

FIGURES

NOMENCLATURE

AFM	Atomic force microscope
AR(C)	Anti-reflective (coating)
BCB	Benzocyclylbenzene
BCP	Block co-polymer
CD	Critical dimension
CMOS	Complementary metal-oxide-semiconductor
DOE	Department of Energy
DPD	Dissipative particle dynamics
DSA	Directed self-assembly
e-beam	Electron beam (lithography)
EUV	Extreme ultraviolet
GMA	Glycidyl methacrylate
hp	Half-pitch
IL	Interferometric lithography
ITRS	International Technology Roadmap for Semiconductors
LER	Line edge roughness
LWR	Line width roughness
NIL	Nano-imprint lithography
NINE	National Institute for NanoEngineering
NMP	N-methyl-2-pyrrlidone
PECVD	Plasma Enhanced Chemical Vapor Deposition
PGMEA	Propylene glycol methyl ether acetate
PMMA	Polymethyl methacrylate
PR	Photoresist
PS	Polystyrene
RIE	Reactive ion etch(ing)
SAM	Self-assembled monolayer
SCCM	Standard Cubic Centimeters per Minute (at standard temperature and pressure)
SEM	Scanning electron microscope
SERS	Surface Enhanced Raman Scattering
SNL	Sandia National Laboratories
UNM	University of New Mexico
UW	University of Wisconsin
VUV-VASE	Vacuum ultra violet variable angle spectroscopic ellipsometer
WGP	Wire grid polarizer

1. INTRODUCTION

The extreme nanoscale features prescribed by the International Technology Roadmap for Semiconductors (ITRS, *e.g.*, 11nm half-pitch for dense patterns and 4.5nm critical dimensions by 2022) require infrastructure-heavy extreme ultraviolet (EUV) and/or alternative lithography approaches.[1] Current 193nm immersion optical lithography can print ~40nm half-pitch and may reach 20nm with double patterning. Recently, the cost of optical lithography steppers has been growing significantly faster than the historical trend in order to keep pace with ITRS CD requirements.[2] This cost is growing so much so that non-optical techniques are becoming viable patterning options. While enormous effort has been invested in extreme ultra-violet (EUV) lithography, persistent doubts remain due to a costly complete change of infrastructure. Therefore, alternative lithographic pathways to the extreme nanoscale ITRS goals are needed. The goal of this project was to explore the possibility to direct the self-assembly of block copolymers (BCP) into device-oriented patterns fabricated by optical interference lithography (IL), use those self-assembled BCP patterns as masks to create nanoimprint lithography (NIL) masters via plasma etching, and fabricate prototype devices using this combined top-down and bottom-up approach.

BCP-based patterning techniques excel at extreme nanoscale feature definition, but have significant questions related to defect density, long range order, and the fabrication of multiple feature types on a single wafer. The initial vision was to use IL-directed BCP to achieve long range order across device-relevant dimensions, and build up a single NIL master from multiple IL+BCP directed self assembly (DSA) coupons, to allow us to fabricate essentially arbitrary patterns of extreme nanofeatures unencumbered by optical diffraction limitations. Extensive metrology associated with relevant characteristics (critical dimensions, line edge roughness, pattern fidelity, defect density and distribution, etc.) at every stage of the process was anticipated to provide guidance about the eventual feasibility of this approach, however difficulties in achieving both reliable IL patterns as well as quality self-assembled patterns limited this component of the project. In spite of the difficulties in integrating these three disparate technologies together, significant progress was made in several areas.

This was one of the flagship projects of the National Institute for NanoEngineering (NINE). NINE was a noble attempt at university, industry, and national laboratory collaboration that was ultimately foiled largely by legal wrangling over potential intellectual property. The purpose of NINE was to bring together the capabilities and expertise of national laboratories and top universities to do pre-competitive research on problems in nanoscience of strong interest to a variety of industrial partners. In addition to the technical outcomes of the NINE projects, there was a strong education and workforce development aspect to both the individual projects and the overall NINE program. In the case of this project, we worked closely with individuals from Intel Corporation early in the project until the industrial aspect of NINE was discontinued. The technical and educational aspects of the projects, however, continued, with collaboration among, for this project, Sandia, Prof. Steve Brueck's research group at the University of New Mexico, and Profs. Paul Nealey's and Juan de Pablo's groups at the University of Wisconsin.

Section 2 contains a brief overview of each of the component technologies (IL, BCP and NIL) as well as some discussion of the integration. Section 3 covers the initial metrology work performed on both IL and BCP line edge roughness. Section 4 gives a brief overview of the BCP simulation. Section 5 covers pattern transfer performed at SNL on both IL and BCP patterns, and section 6 covers two proxy applications that demonstrate successful combination of the component technologies. Section 7 offers some conclusions. Both for brevity and out of respect for the majority of this work, which has or will be published in peer-reviewed journals, this report is meant only as a general overview. Readers interested in greater technical detail are pointed to the extensive references within this work as well as the recent and upcoming publications from all collaborators, in particular the University of Wisconsin groups.

2. COMPONENT TECHNOLOGIES

2.1 Overview

The International Technology Roadmap for Semiconductors (ITRS) prescribes an 11nm half-pitch (hp) for dense patterns and 4.5nm critical dimensions (CDs) by 2022.[1] Current 193nm immersion optical lithography can print to ~40nm hp and may reach 20nm hp with double patterning. Block copolymer (BCP)-based patterning represents one of the few potentially feasible approaches for commercialization at the sub-20nm scale, but BCP lithography alone lacks flexibility in handling variable pattern densities and multiple feature sizes, and offers poor long-range order—all requirements for integrated circuit devices. Nanoimprint lithography (NIL, Figure 2.1) is a top-down technique that transfers features from a template through direct contact instead of through photons. Unencumbered by diffraction limitations, NIL does not require the complex light sources and optics that increase the cost and complexity of photolithography, has demonstrated reproduction of features as small as 5nm, and can provide acceptable alignment and overlay accuracy.[3] NIL, however, requires that the nanoscale features that it imprints initially be defined using some other approach.

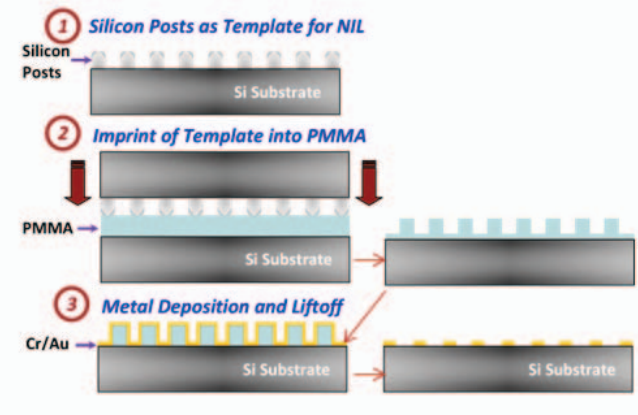

Figure 2.1. NIL can pattern predefined features at the extreme nanoscale.

Chemically-directed BCP lithography can guide polymer self-assembly into large area, nearly defect-free patterns with 5-50nm dimensions, and can multiply the feature density while improving the pattern quality by reducing the CD variability and LER.[4-6] Currently, slow and expensive e-beam or extreme ultraviolet (EUV) lithography is used to form sub-100nm chemical pre-patterns for directing BCP assembly. We use relatively inexpensive immersion 193nm optical interference lithography (IL) to pre-pattern substrates for directed BCP assembly over large areas where aggressive periodic nanoscale features are required. Traditional lithographic processes (optical and/or e-beam) can be used to personalize the pattern by integrating adjacent features at lower resolution. Since multiple IL+BCP coupons can be combined to form a single NIL master, the resulting NIL-patterned samples can, from a single imprint step, exhibit a wide variety of different feature sizes and shapes, all with potentially sub-20nm sizes and long-range order defined by the initial IL patterns (see Figure 2.2 for a general schematic diagram of the concept).

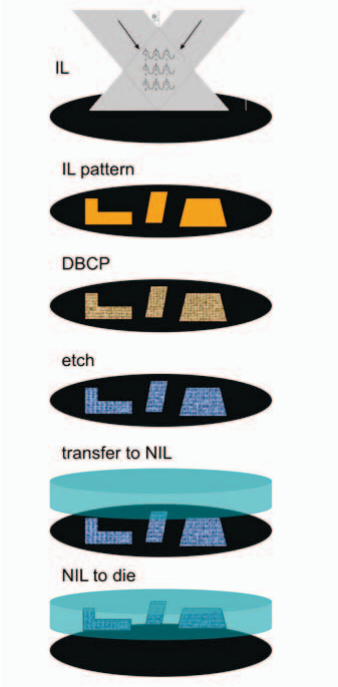

Figure 2.2. Schematic outline of the proposed patterning hybrid lithography scheme.

The fundamental limits of BCP patterning techniques, in terms of ultimate minimum feature size as well as coupled parameters such as annealing time and defect density, are largely unknown. Extensive metrology associated with critical characteristics (CD, LER, pattern fidelity, defect density and distribution, etc.) at every stage of the process provides guidance about the eventual feasibility of this approach. Further, fabrication of carefully-designed prototype device structures gives us not only a demonstration of the capabilities of the techniques, but also an additional method for characterizing the quality of the patterning and eventual materials structures. Coupling this extensive experimental data with molecular modeling and simulation which takes into account not only the effects of the substrate surface and other interfaces on thermodynamic stability but also kinetic contributions to morphology gives us a powerful suite of tools for evaluating the fundamental limits and coupled processing parameters associated with BCP-based lithography.

Integration of directed BCP assembly with NIL introduces a bottom-up self-assembly technique into electronic and photonic device fabrication and provides a solution to practical production of NIL templates compatible with the future demands of the ITRS. This project is the first combination of IL with BCP and NIL technologies, and will define the limits of a combined top-down/bottom-up lithography approach for use in commercial applications including integrated circuit manufacture.

2.2 Immersion Interferometric Lithography

Immersion Interference Lithography is a large area, rapid, low cost lithography technique for patterning nano-periodic structures with flexible morphology.[7] Figure 2.3 contains a schematic diagram of the IL setup we will use to create patterns to direct the BCP assembly. It

consists of a photoresist-coated wafer coupled to a prism with water. Coherent beams are directed into the resist and their interference results in a latent image where high intensity regions in the resist are de-protected, allowing their selective removal by a developer. The pitch of the lines is controlled by the angle of incidence of the two beams as well as the index of the material in which the interference occurs. In this case, we chose 2 different prisms with AR coatings resulting in 90 nm and 82 nm pitch lines.

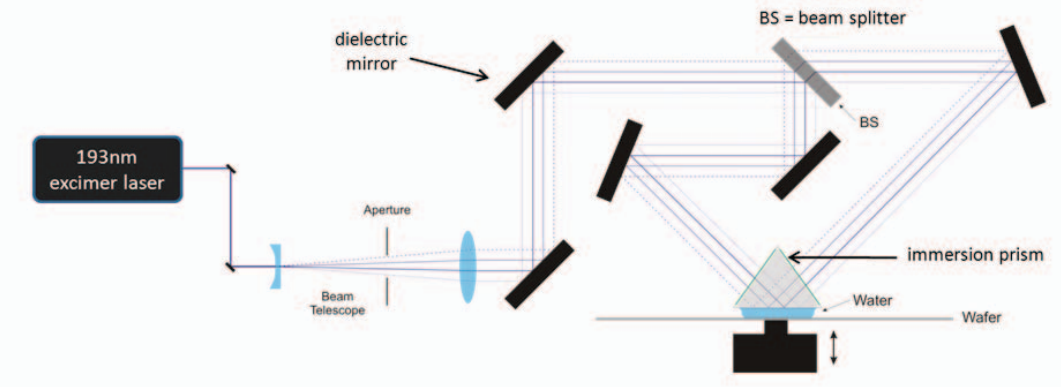

Figure 2.3. Schematic of the Immersion Interferometric Lithography exposure setup.

Because the source is coherent, standing waves typically form in the resist where the portion of the incident beam that reflects off the substrate interferes with the incident beam. At a minimum, this behavior can lead to scalloping on the edges of the photoresist lines. In extreme cases, it can result in line collapse. In any event, standing waves are a bigger problem for the smaller pitches relative to the exposure wavelength. In many circumstances, an absorptive organic anti-reflection coating (ARC) can be deposited beneath the photoresist. This layer combines bulk absorption with thin film optical interference effects to attenuate the exposing light that passes through the resist and preventing back reflection.

For this work, the IL pattern is used to make a chemical pattern in the cross-linked polystyrene mat. The thickness of the IL resist was inadequate to transfer through the organic ARC layer, resulting in incommensurate line-space ratios during creation of the chemical pattern required for directed BCP assembly (Figure 2.4, top). The result was that we chose two different inorganic layers to use as purely dielectric thin film ARCs (Figure 2.4, bottom). These layers work by imparting an optical phase shift in the exposure light that passes through the resist such that the reflected light is out of phase with the incident light, and reflection is minimized. We chose two CMOS-compatible inorganic films to study: Si_3N_4 and later SiO_2.

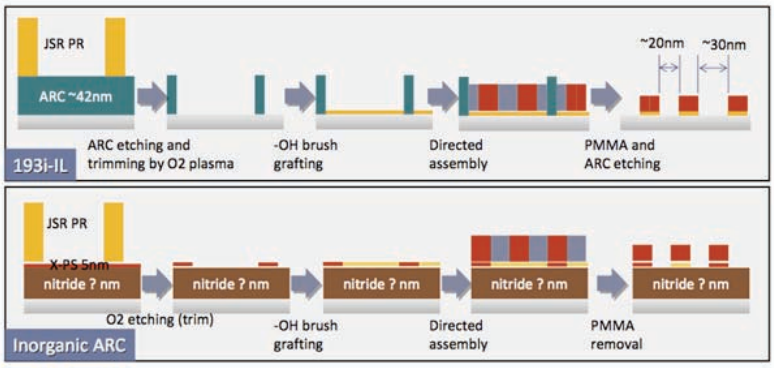

Figure 2.4. Schematic showing the processing differences between using an organic ARC (top) and an inorganic ARC (bottom).

The IL exposure is extremely sensitive to the optical stack under the resist. Without an absorbing ARC, even the presence of the thin PS brush layer must be taken into account. Spectroscopic ellipsometry is a highly sensitive measurement technique capable of measuring the optical constants of a material by measuring the polarization state of incident and reflected light and comparing these results with a model system. In order to ease the difficulty of measuring these extremely thin films, the film stack was measured piecewise, first with an inorganic nitride film to assess those properties and then with a nitride/PS stack measure the PS film. Silicon wafers with low and high stress PECVD-deposited nitride were shipped to J.A. Woollam to measure the n and k parameters at the exposure wavelength (193nm) using a vacuum ultra violet variable angle spectroscopic ellipsometer (VUV-VASE). Figure 2.5 a.) contains the graph of n and k versus wavelength. With the optical parameters of the nitride layer fixed, the PS film was applied to the wafer, and the wafer was measured again. The optical constants for the PS film are shown in Figure 2.5 b.). With these material parameters established, optimal thicknesses for the film stack were calculated using standard thin film reflectivity calculations. The results of these optimizations are shown in the reflectivity plots in Figure 2.6: 12 nm for Si_3N_4; 33 nm for SiO_2.

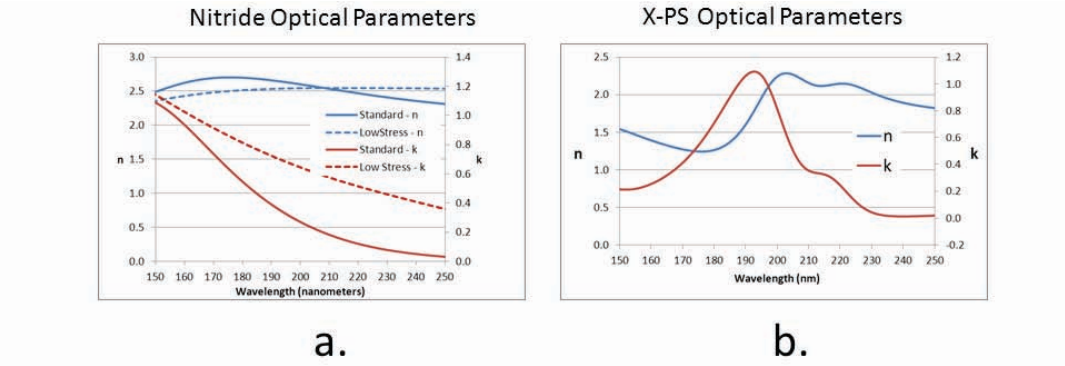

Figure 2.5. Graph of the optical constants (n and k) for both the standard SNL nitride and the low stress nitride.

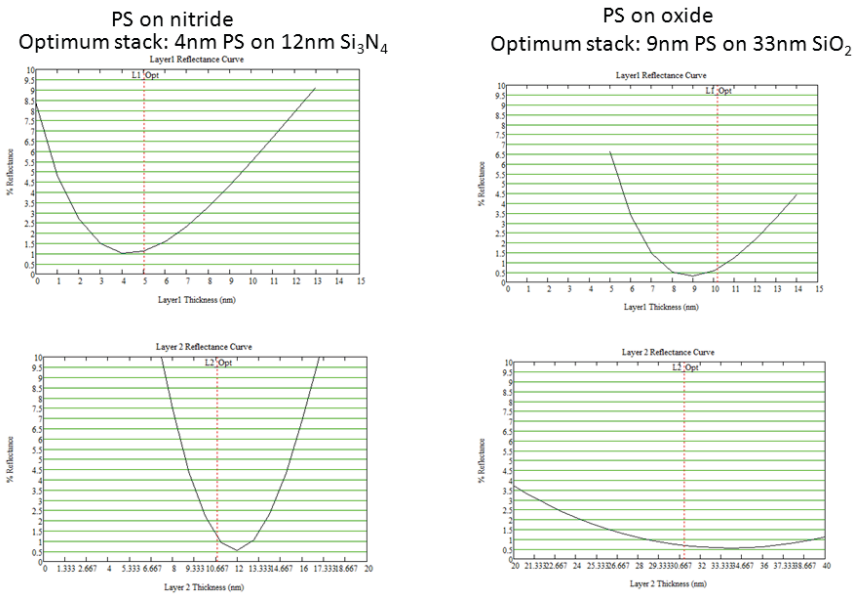

Figure 2.6. Plot of reflectivity using standard thin film calculations to optimize ARC stack.

Figure 2.7 a.) shows an optical image of a typical exposure after development. The 82 nm line spacing of the grating is below the diffraction condition for visible light, however two distinct regions are apparent from this image: the tan colored lower left region containing resolved lines, and the blue colored region in the upper right corner containing unresolved lines. Figure 2.7 b.) shows an SEM image of well-resolved lines.

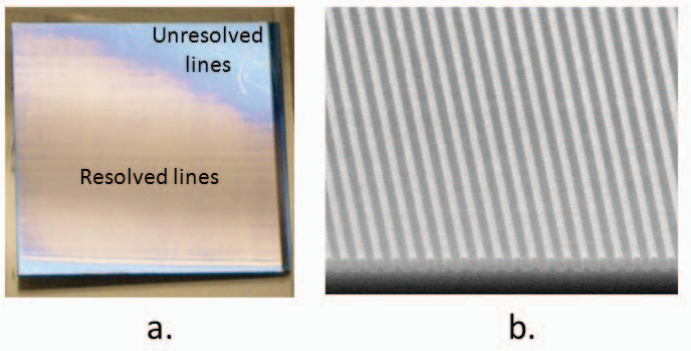

Figure 2.7. a.) Optical image of an IL exposed sample; b.) SEM image from the "Resolved-lines" region of the sample.

The macroscopic non-uniformity across the sample was attributed to excimer laser beam non-uniformity due to slightly damaged inter-cavity optics. Nevertheless, both 82 nm and 90 nm lines were resolved over multiple square-cm areas, more than enough space to demonstrate proof-of-concept, long range directed assembly. Figure 2.8 shows a matrix of SEM images taken at intervals over a $1cm^2$ area (optical image of sample, left), demonstrating good uniformity over this range.

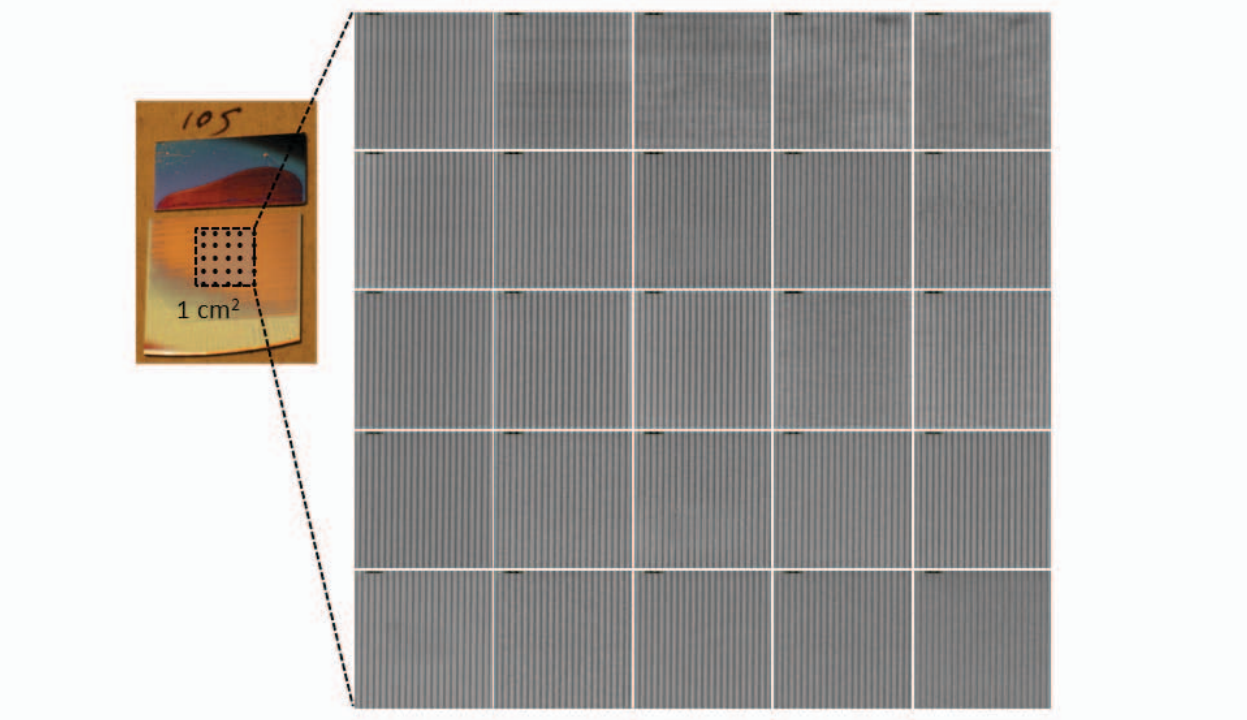

Figure 2.8. Matrix of SEM images captured over 1 cm^2 area of IL patterned sample (optical image, inset left).

2.3 Directed Self-Assembly of Block Co-polymers

Block copolymers are composed of two polymeric chains (blocks), which are chemically different and covalently attached to each other. The different polymer chemistries segregate into ordered structures that minimize the interface between blocks with the constraint that the blocks are covalently bonded. This self-assembly process forms dense, periodic structures such as spheres, cylinders or lamellae, depending on the volume fraction of the blocks. A typical pattern of self assembly termed the "fingerprint" pattern is shown in Figure 2.9. In this image the PMMA block has been selectively removed to show the contrast between the two polymer domains. While these random patterns are mesmerizing to look at, in order to use BCP self-assembly to create non-random, device-like patterns, the forces which control and drive the self-assembly process need to be harnessed.

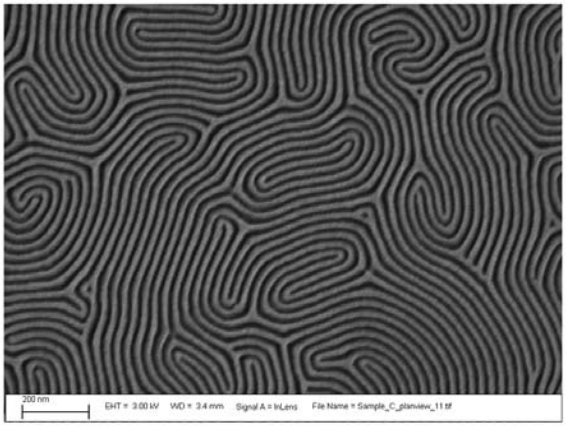

Figure 2.9. SEM image of a fingerprint pattern resulting from self-assembled PS-b-PMMA BCP patterning. The PMMA block has been removed to increase the contrast.

Directed self-assembly (DSA) of block copolymer (BCP) films is a patterning technique that has the ability to increase the density of features compared to those defined in a single exposure while at the same time offering decreased process complexity and therefore lower cost than double patterning. Feature density multiplication schemes incorporating BCP DSA have been successfully demonstrated using e-beam, extreme ultraviolet (EUV), or 193i lithography.[4-6]

The directed self-assembly (DSA) of block copolymers (BCP) is coupled with a top-down lithography technique to improve the pattern quality and/or resolution. In general, two approaches can be used to control the alignment and placement of BCPs: graphoepitaxy and chemoepitaxy. Graphoepitaxy involves topographic patterns that use spatial confinement effects to direct BCPs while chemoepitaxy involves chemical patterns that have regions with different wetting properties.

Chemical patterns designed for directed assembly of block copolymers often have been fabricated from a homogeneous thin organic film that was lithographically patterned and subsequently etched with an oxygen plasma to remove, either completely or partially, the film material in selected areas. The initial film was formed from self-assembled monolayers (SAMs), polymer brushes, or polymer mats. The etched regions of the film would be wet preferentially by one block of the copolymer, while the unetched regions would either be wet by the other block or be nonpreferential in wetting toward the two blocks. (The region with a strong preference to be wet by a specific block of the copolymer is referred to as the guiding region and the second region, which usually has an area greater than or equal to the guiding region, as the background region.) Because the guiding and background regions were derived from the same initial thin film, their chemistries could not be chosen independently. Moreover, the chemistry of the guiding regions was dependent on the etching conditions, and the chemistry of the protected regions could also be affected by the lithographic and etch processes.

The need for increasingly precise control of chemical pattern feature dimensions and chemistry has been highlighted by recent directed assembly results in which the assembled block copolymer feature density was an integral multiple of the chemical pattern feature density. This increase in feature density, known as “density multiplication,” yields an assembled pattern with greater resolution than the original, lithographically defined chemical pattern. Ruiz *et al.* and

Detcheverry *et al.* used both experiments on and simulations of polystyrene-block-poly(methyl methacrylate) (PS-b-PMMA) directed to assemble with density multiplication on chemical patterns composed of hydroxyl-terminated polystyrene (PS-OH) brush, which had been patterned and subsequently oxidized.[5,8] If the dimensions of the guiding regions of the block copolymer deviated significantly from the size of a block copolymer domain, or if the background chemistry were not optimum, defect-ridden assemblies or complex three-dimensional structures formed. Even in directed assembly without density multiplication, Edwards *et al.* demonstrated that the geometry and chemistry of the chemical pattern can affect the assembly dynamics, the three-dimensional structure of the assembled domains, and the uniformity and perfection of the equilibrated, assembled pattern.[9]

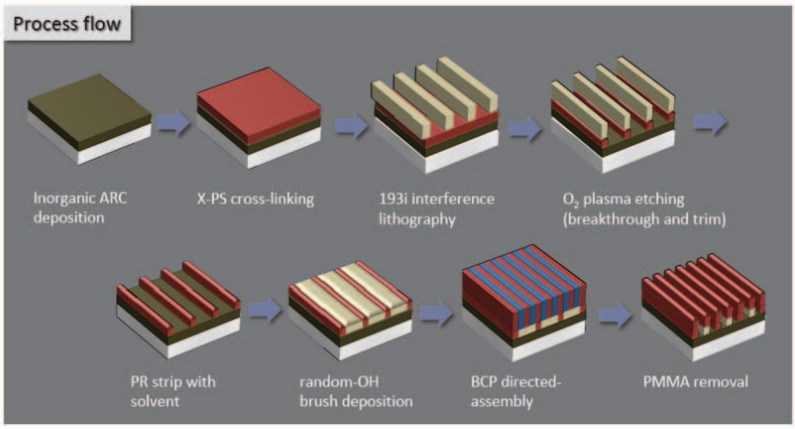

Figure 2.10. Schematic of the process flow to create density multiplied features via interferometric lithography and directed self assembly (figure adapted with permission from the American Vacuum Society).[10]

The chemical pattern fabrication method used in this work features precise control in chemistry and geometry utilizing specialized materials and lithographic patterning techniques. This process is shown schematically in Figure 2.10. The principal idea involves two steps: (1) create a base imaging layer that retains its chemistry through processing but can be patterned by lithography and a sublithographic trim etch and (2) selectively deposit materials in the interspatial regions where the base imaging layer was removed after patterning. The process starts with the formation of a cross-linked polymer mat on the substrate, which is lithographically patterned and subsequently etched to expose the substrate in desired locations. Hydroxyl-terminated polymer brushes are then deposited and grafted to the exposed substrate to fill the interspatial regions. Importantly, throughout the entire process the chemistry of the polymer mat remains unchanged due to its high degree of cross-linking. Not only do the materials and process provide precise control of both the chemistry and the geometry of the chemical pattern, but they allow greater freedom in the choice of materials.

Because the BCP film is composed of two polymer species, the chemical pattern providing the guiding force for self-assembly can be either PS or PMMA. From DSA results on cross-linked PS (X-PS) or cross-linked PMMA (X-PMMA) guiding stripes with the PS content of the brush varying, it is possible to ascertain the optimal PS:PMMA ratio for a given guiding stripe. Using the optimal conditions for X-PS guiding stripes (43% PS), large area density multiplication was achieved using e-beam written patterns. Figure 2.11 shows successful density

tripling in trim-etches lines with optimal brush fill factor. Integration of feature density multiplication via directed assembly of a BCP with 193i lithography provides pattern quality that is comparable with existing double-patterning techniques. Thus, if carefully combined with design for manufacturing, directed assembly could be a promising candidate for extending the use of current 193i lithography tools to higher pattern densities and for lowering the overall patterning cost.

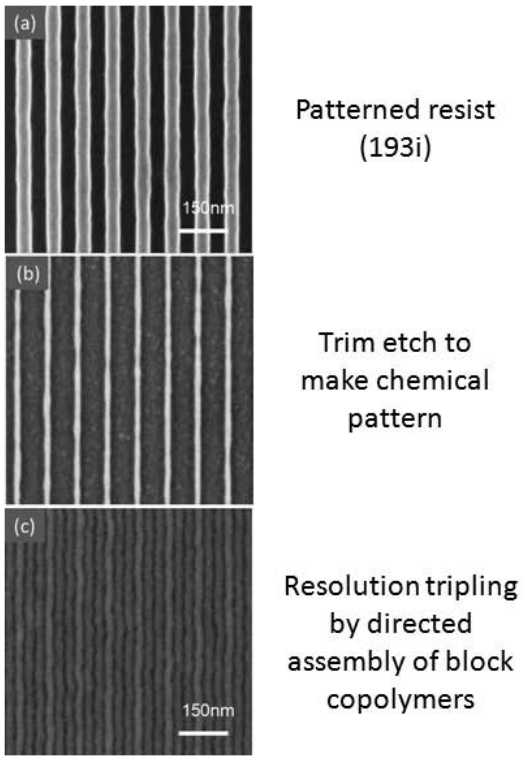

Figure 2.11. a.) SEM image of patterned resist; b) SEM image of trim etched lines to optimal fill factor for density multiplication; c) SEM image of DSA BCP lines on pattern showing clear density multiplication.

One of the integral components needed for directed self-assembly (DSA) of block copolymers (BCP) is a preferential stripe in the chemical pattern, which is preferentially wet by one of the blocks to guide the BCP assembly. In this project, we have focused on developing DSA patterns for polystyrene-b-poly(methyl methacrylate) (PS-b-PMMA) BCP using a PS preferential stripe. An assortment of PS-based materials were tested for application as the preferential stripe in a 2:1 density multiplication scheme, assembling PS-b-PMMA 37k-37k BCP (L_0 = 40 nm) on an 82 nm pitch line array generated from 193i interference lithography.

Successful fabrication of a DSA chemical pattern requires the PS film to meet several process specifications. For one, the PS layer must be insoluble to solvents and developers used after it is deposited. This can be accomplished by tethering the film to the substrate and/or cross-linking the PS (x-PS). Also, it must be integrated into the antireflective stack to satisfy the photoresist patterning requirements. PS is highly absorptive and reflective at the 193 nm wavelength, so it is sensitive to film thickness and must be combined with a transparent

inorganic layer in order to minimize back reflections into the photoresist. Finally, the PS layer must be non-fouling, with both the photoresist and the backfilling polymer brush.

Several different PS-based materials were tested as the PS layer. Hydroxyl-terminated polystyrene (PS-OH) can be grafted to surface hydroxyl groups through a condensation reaction. Steric hindrance limits the grafting density of a saturated brush. Alternatively, the PS was copolymerized with a small amount of a crosslinking monomer that thermally crosslinks. Two crosslinkers were used in this study: glycidyl methacrylate (GMA) and benzocyclobenzene (BCB). The GMA monomer unit is able to both crosslink and graft to the surface hydroxyl groups above 160°C. On the other hand, the BCB monomer begins to crosslink above 200°C with no reaction to the surface. The BCB-based PS was synthesized with both hydroxyl-termination and without, facilitating more precise comparison between a tethered and untethered crosslinked PS film.

Si wafers with a specified film of silicon nitride or silicon oxide were provided by Sandia National Laboratories cleanroom facility. Hydroxyl-terminated polystyrene (PS-OH, Mn = 10 kg/mol) and symmetric block copolymer PS-b-PMMA 37k-37k were purchased from PolymerSource. Crosslinkable PS synthesized at the University of Wisconsin consisted of 4% GMA in PS (PS-GMA4) or 7% BCB in PS with hydroxyl termination (PS-BCB7-OH). Crosslinkable PS synthesized by AZ Chemical consisted of 3% BCB in PS (PS-BCB3) or 11% BCB in PS (PS-BCB11).

In order to form end-grafted PS guiding stripes, a 1% solution of PS-OH was spin-coated onto a nitride-coated silicon wafer. The sample was heated to 190°C for 24 hr under vacuum conditions to graft the polymer chains to the surface. Ungrafted PS-OH was removed by sonicating three times in toluene for 5 min. In order to form crosslinked PS guiding stripes, a dilute solution of x-PS in toluene or PGMEA was spin-coated onto a silicon wafer, yielding a film of 4-10 nm in thickness, depending on the antireflective stack being used. The sample was heated to 190°C for 24 hr under vacuum conditions or 250°C for 5 min under nitrogen environment to drive the cross-linking reaction.

Following deposition of the appropriate PS layer, chemically amplified photoresist (JSR ArF ARx2928JN-8) was spincoated at 2500 rpm, resulting in an 80 nm thick layer on the x-PS followed by a post-applied bake at 120°C for 90 s. The photoresist was subsequently patterned with 193i interference lithography. After the post-exposure-bake at 115°C for 90 s, the sample was developed for 60 s with Futurex RD6 followed by a 15 s deionized water rinse and a 3 s surfactant rinse (0.01% DuPont Zonyl FSO-100 in de-ionized water). The final structure in the photoresist was a grating pattern consisting of parallel lines with a period, L_s = 82 nm. The samples were etched with an oxygen plasma (75 mT, 8 SCCM O2, and 100 W in a PlasmaEtch PE-200 tool) to remove the x-PS or PS-OH in the non-photoresist-covered region and to decrease the width of the photoresist stripes. The photoresist was then removed with a warm solvent (NMP) and with repeated sonication. Hydroxyl-terminated P(S-r-MMA) was spin-coated from a 0.5 wt% toluene solution at 3000 rpm onto the samples. The substrate was then baked at 190°C for 4 h or 250°C for 5 min to graft the P(S-r-MMA)-OH onto the nitride/oxide used in the ARC stack, resulting in a 5-nm-thick layer of P(S-r-MMA). Excess P(S-r-MMA) was washed away with toluene and sonication after the reaction. The PS-b-PMMA was spin-coated from a 1.5 wt%

solution in toluene at 4000 rpm, resulting in a 40-nm-thick film, which was then annealed for 5 min at 250°C in a nitrogen environment.

In addition to satisfying the optical properties, the PS film must be non-fouling by the photoresist and the backfilling brush. Water contact angle was used to demonstrate that the photoresist was removed cleanly from all PS surfaces by rinsing with NMP. However, the each of the PS materials responded to the backfilling process differently. Polymer brushes have a saturation limit on the grafting density based on entropic limitations. This saturation point leaves many unreacted surface sites, and since the individual chains of the brush are not connected, they do not completely shield the surface from the backfilling polymer chains spin-coated on top. This means that some backfilling chains are able to graft into the preferential stripe, thus reducing the chemical contrast between the guiding stripe and the background. The reduced contrast leads to significant increase in defect density compared to a PS-GMA4 crosslinked film, as seen in Figure 2.12.

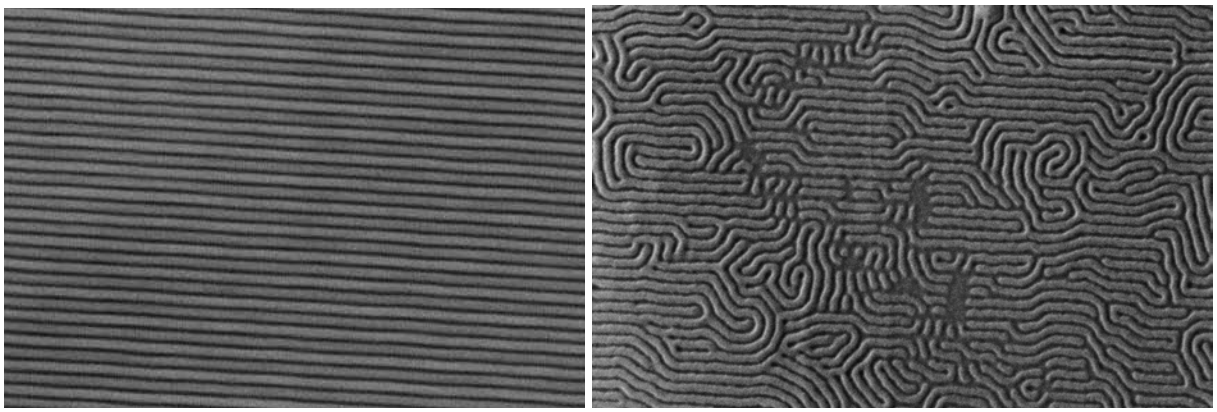

Figure 2.12. Assembly of 37k-37k (L_0 = 40 nm) on an 82 nm chemical pattern, where the same processing was used except a) PS-GMA4 guiding stripes and b) PS-OH guiding stripes.

To mitigate the interpenetration, the previously described process was modified to use the photoresist to block the interpenetration of the backfilling polymer. Figure 2.13 demonstrates the process steps through schematics and plain-view SEM. Despite the resist dewetting during the anneal process, it should still block some of the interpenetration. However, it did not show any improvement to the block copolymer assembly. Further optimization of this process is not expected to make enough difference to generate a chemical pattern comparable to the PS-GMA4 pattern.

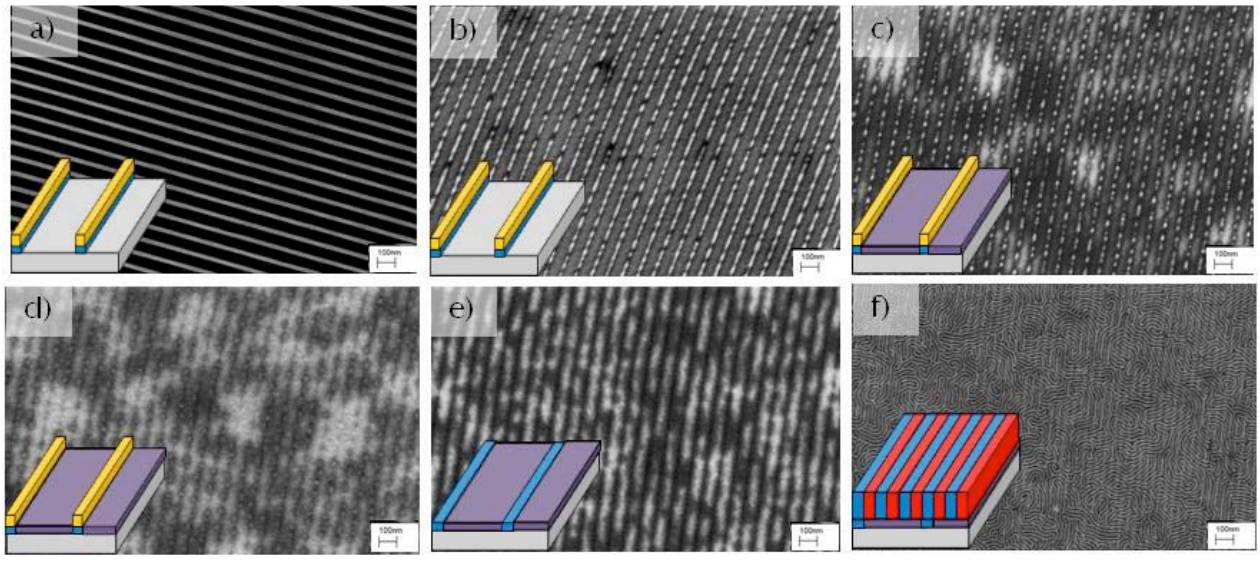

Figure 2.13. Steps through the process of using PR to prevent interpenetration a) trim etch PR with O_2 plasma, b) switch solubility, c) spincast brush, d) graft brush, e) remove PR, f) assemble block copolymer.

Not only is it important that the PS film is crosslinked, the choice of crosslinker also affects the ability to generate a quality chemical pattern. One motivation to replace the GMA crosslinker is that the expoxy ring is unstable in solution, as it is opened with trace amounts of water. A solution of the polymer in toluene has a shelf life of a few days. Using a crosslinker with different characteristics is useful to demonstrate the important properties of the polymer film. Compared to GMA, BCB has a chemical structure more closely resembling that of PS, so the affinity for the guiding stripe could be stronger. Also, BCB cannot graft to the substrate in the way that GMA can. However, the polymer can be tethered to the surface by including hydroxyl termination, just like the brush polymer chemistry.

As demonstrated in Figure 2.13 and in other studies, chemical patterns made from PS-GMA4 are able to assemble PS-b-PMMA block copolymers through the density multiplication process consistently. In contrast, the BCB-crosslinked films showed more complex behavior. Specifically, the PS-BCB-OH polymer could be used to make successful chemical patterns when spincast from toluene, but without the surface tethering, both crosslinker loadings of PS-BCB could not. Further analysis showed that the hydroxyl-terminated backfilling polymer could graft to unpatterned PS-BCB films. This is not the same interpenetration problem that was described with the PS-OH system since the backfilling polymer grafted on top of the x-PS, increasing the film thickness by the saturation thickness of the brush. Also, insufficient crosslinking does not explain the results, as the crosslinker loading was varied from 3% to 11% by mixing the PS-BCB polymers and this bounds the 7% BCB loading that is in the PS-BCB-OH. Furthermore, increasing the crosslinking annealing time up to 30 min did not change the fouling properties. The PS GMA4 and PS-BCB-OH crosslink sufficiently to prevent interpenetration with less than 5 min of annealing at the same conditions (350°C).

In addition to changing the crosslinker, the choice of spincasting solvent also influences the quality of the resulting film. Casting PS-BCB-OH from toluene generates a quality pattern,

as mentioned previously. If the solvent is switched to PGMEA, a solvent that is widely used in the semiconductor industry and has lower safety hazards, the resulting film has the same fouling issues as the PS-BCB films. While the mechanisms responsible for the observed differences between the types of PS films described here were not investigated in detail, these experiments do highlight important aspects of the chemical pattern fabrication process, including the significance of x-PS grafting to the substrate and the choice of casting solvent. More work is needed to understand why the backfilling brush grafted to the x-PS and how the choice of solvent affects the properties of the x-PS film.

2.4 Nano-Imprint Lithography

There are two basic process steps in thermal nano-imprint lithography. First is the imprint process in which a template with predefined nanostructures on its surface is pressed into a photoresist thin film layer that has been spun-cast onto a substrate (Figure 2.14a), followed by the removal of the template (Figure 2.14b). The nanostructures on the template surface are replicated in the resist film during this first step. The second step involves the transfer of the imprinted pattern into the entire thickness of the photoresist by an anisotropic reactive-ion etching (RIE) in a plasma environment that removes the residual resist in the compressed area (Figure 2.16c). During the imprint process, the photoresist is heated to a temperature that is above its glass transition temperature. The resist becomes a viscous liquid at the elevated temperature, reflows and conforms to the shape of the imprint template, and eventually hardens as the temperature decreases.

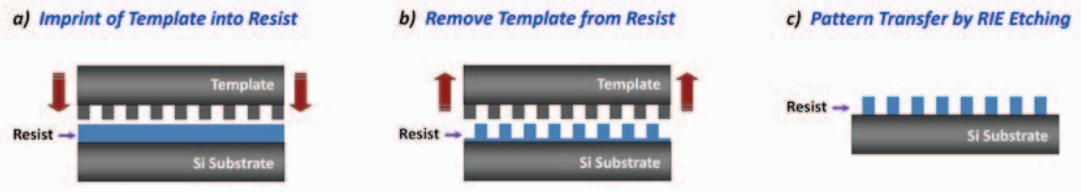

Figure 2.14. The basic process steps to nanoimprint lithography include a) imprinting the template into a photoresist thin film, b) removing the template from the photoresist, and c) transferring the pattern into the entire thickness of the photoresist by an anisotropic RIE etch.

Nano-imprint lithography does not utilize energetic light beams and therefore is not limited in resolution by the effects of diffraction, scattering and interference in the photoresist, or back-scattering from the substrate that are common to conventional lithography techniques.[11] The templates used in nano-imprint lithography can be fabricated with high-resolution techniques such as electron beam lithography or, as shown here, BCP-based techniques.

Because nano-imprint is a physical process that involves mechanical contact between a template and a substrate, pressure uniformity between the two elements is important in achieving adequate process control. Solid parallel plate presses used in traditional thermal imprint tools have the inherent problems of non-uniform pressure distribution as well as relative shift motions between the template and substrate due to the surface roughness and parallelism of the plates.[12] In order to achieve acceptable critical dimension (CD) control, the residual photoresist thickness after the imprinting process should be uniform, the relative movement during mechanical contact

should be minimized to increase overlay accuracy, and a conformal contact between the template and substrate is required since they are not perfectly flat.

The nano-imprint lithography tool (Nanonex NX-2000) utilized in this work was developed by Nanonex to overcome the pressure uniformity challenges as well as the inherent problems associated with parallel plate presses. The Air Cushion Press technology used in Nanonex NIL tools achieves conformal pressure uniformity by applying a constant hydrostatic air pressure around the entire template-substrate stack and is capable of handling substrates with uneven backing surfaces as well as curved samples.

The Nanonex NIL tool is capable of producing 10 nm line-width features with a 30 nm pitch in the photoresist layer from an electron-beam generated imprint template. One of the issues with creating a usable imprint template is that the features must have the correct profile to allow removal of the imprint polymer from the master. Figure 2.15 shows two different taper profiles that can result from etching. During imprint removal, the inverse-tapered geometry on the left (SEM image in lower left is an example of this issue) locks onto the imprint master so that either the polymer is fused to the master or excessive force is required to release the stamp, causing damage to the master. The profile on the right with a positive-taper does not suffer from this difficulty, allowing the stamp to be removed from the master.

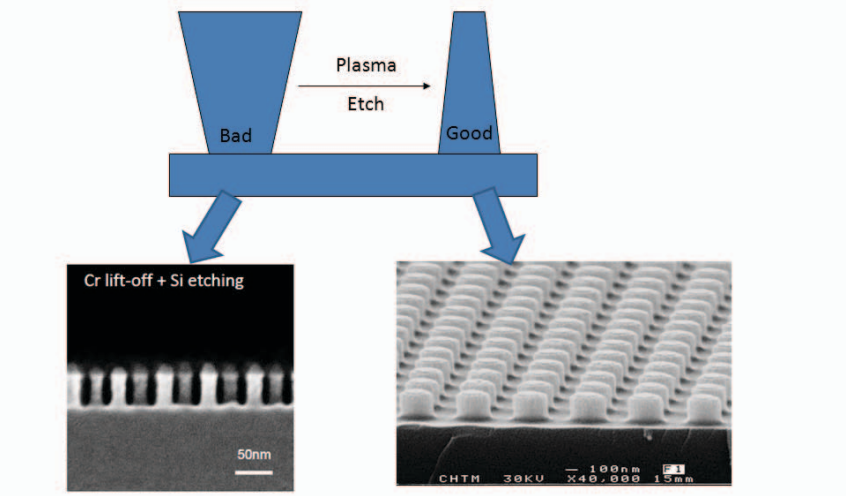

Figure 2.15. Schematic diagram (top) and SEM images showing sub-optimal mold profile with negative taper (left) and optimal mold profile release with zero to positive side wall taper (right).

Nano-imprint lithography using block-copolymer templates is a manufacturable solution for nanoscale lithography. Block-copolymers present a self-assembly based approach toward rapid nanoimprint template production with no need for complex machinery. Typically, periodic domains formed by the phase separation of two or more dissimilar polymers are on the order of 5–50 nm in size, but can be significantly extended by directing the self-assembly (see earlier discussion in this repot and associated references).

Using an integrated BCP-NIL process, a nanoimprint template was fabricated by using the self-assembly of a diblock-copolymer [poly(styrene-*block*-methyl methacrylate) (PS-*b*-PMMA)] to form an etching mask for the creation of posts on a silicon wafer. This template in

turn was used in a nanoimprint pattern transfer to create a photoresist layer with holes. Metal deposition and lift-off resulted in an array of Au nanodots measuring 20 nm in diameter. These nanodots were subsequently shown to produce an enhancement in the Raman scattering signature of Rhodamine 6G (R6G) interrogation molecules in a prototype surface-enhanced Raman spectroscopy (SERS) device. To the authors' knowledge, only one group has demonstrated a similar integrated approach of using block-copolymers to create a silicon template for nanoimprinting. They were successful in fabricating 30 nm pitch magnetic dot arrays for the purpose of magnetic media.[13] An analogous idea was carried out in another group by employing the self-assembly of anodic aluminum oxide templates for nanoimprint lithography.[13] Other than these two groups, the only other related work found involved using nanoimprint as a physical pre-pattern tool for the self-assembly of diblock-copolymers.[15,16] The work presented here is the first to apply the integrated BCP-NIL fabrication method to create a working device, namely, a SERS device.

The fabrication procedure involves a series of two pattern transfers. First, a directed block-copolymer assembly is utilized to form an array of perpendicularly-oriented PMMA cylinders in a PS matrix. This pattern is transferred to a silicon substrate via lift-off and plasma etching, resulting in an array of silicon posts. These posts are used in a second pattern transfer via nanoimprinting to a layer of photoresist. An array of holes is produced in the resist, and this pattern is used to fabricate the SERS device.

The diblock-copolymer self-assembly uses thin films of PS-*b*-PMMA. The fabrication process is illustrated in Figure 2.16. First, a hydroxyl-terminated random copolymer brush layer was deposited on a 4-inch silicon substrate. Then, a thin film (35 nm) of the block-copolymer (PS-*b*-PMMA) was spun onto the substrate and annealed under vacuum to initiate self-assembly. The result was hexagonal arrays of perpendicularly oriented PMMA cylinders in a PS matrix. The PMMA domains were then selectively removed with UV exposure and subsequent glacial acetic acid exposure. Details of this diblock-copolymer self-assembly process are described elsewhere in this report. Chromium (measuring 15 nm in thickness) was evaporated onto the exposed underlying Si and remaining PS matrix. Lift-off in a piranha solution removed the PS and left hexagonal arrays of Cr nanodots to serve as an etch mask for the subsequent dry plasma Si etch. An inductively coupled plasma reactive ion etch (using C_4F_8, SF_6, and Ar with a power of 60 W) was performed to transfer the pattern into the silicon substrate. The resulting silicon posts shown by the scanning electron images in Figure 2.17 have dimensions of approximately 20 nm in diameter, 40 nm in pitch, and 44 nm in height. The sidewalls are approximately vertical and the posts are circular in cross section. Because the BCP assembly was not directed by underlying chemical or geometric patterns in this case, the hexagonal patterns reside in larger "grains" and structural defects could be attributed to imperfections in the self-assembly process.

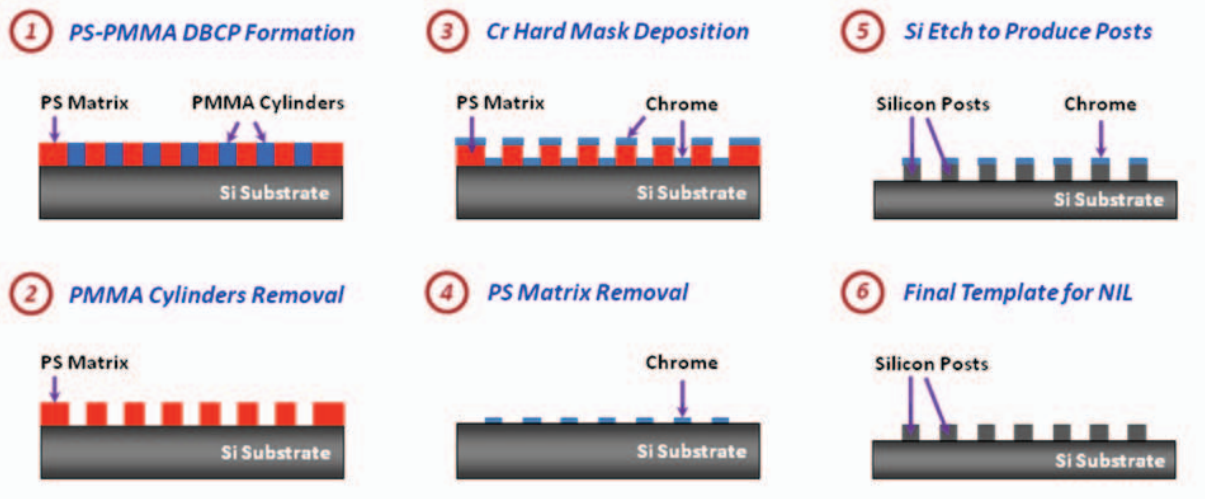

Figure 2.16. Fabrication procedure of silicon NIL templates by block-copolymer self-assembly (figure reprinted with permission from the American Vacuum Society).[50]

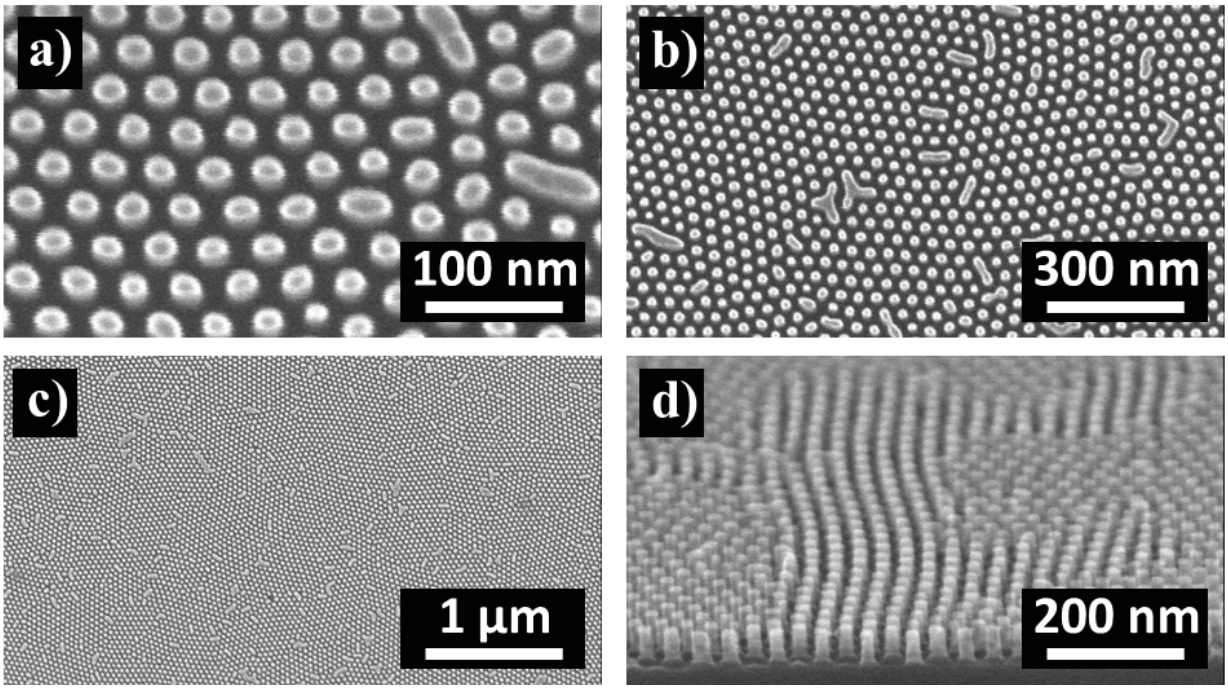

Figure 2.17. a) – c) Top view and d) tilted view SEM images of silicon posts from a NIL template made by block copolymer self-assembly (figure reprinted with permission from the American Vacuum Society).[50]

The silicon template was employed in a nanoimprint pattern transfer. The fabrication process is illustrated in Figure 2.18. A diluted solution of PMMA was spun onto a separate 4-inch silicon wafer to a thickness of approximately 50 nm. A thermal imprint was performed at 200°C and 400 psi for 5 minutes. SEM images of the imprinted PMMA resist are shown in Figure 2.19. The small holes seen in the imprint are a result of successful pattern transfer. Larger voids were formed with nominal diameters of 150 nm. The origin of these larger voids is

still not well understood and is speculated to be either gas bubbles originating from the dilution of the PMMA or areas of PMMA that delaminated during the pattern transfer step.

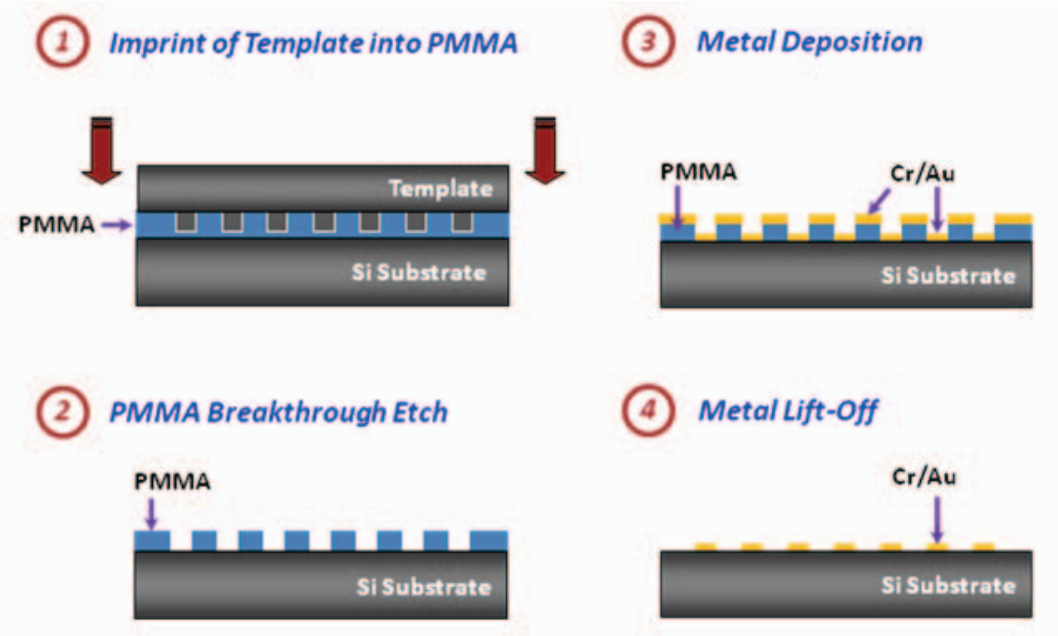

Figure 2.18. Fabrication procedure of SERS device by nanoimprint lithography (figure reprinted with permission from the American Vacuum Society).[50]

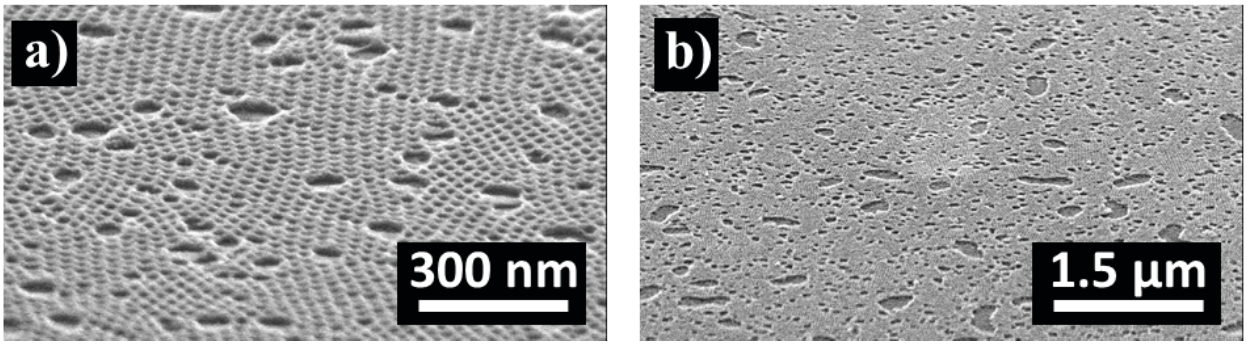

Figure 2.19. Tilted view SEM images of PMMA nanoimprinted sample from the block-copolymer NIL template (figure reprinted with permission from the American Vacuum Society).[50]

3. METROLOGY

All CD measurements used the state of the art FEI Magellan Extreme High Resolution SEM, with a resolution of <0.9 nm at a 1kV acceleration voltage. The Magellan also allows for beam deceleration for surface imaging and contrast without coating the samples, which is critical for in-situ process monitoring. Even with the capabilities of the FEI Magellan, imaging uncoated polymeric structures at these dimensions is challenging, resulting in blooming and line shadowing which make it difficult to determine the exact location of the edge of a line, which is critical for determining CD, LER and LWR. In order to calculate the LER for the samples, a variation of the Patsis procedure was used.[17] First an adaptive 2D noise filter was applied to the images. Next the background non-uniformity was calculated and removed. A threshold was applied to the image and small and large objects were morphologically removed. At this point the edge pixel locations are unambiguous. The edges are found, tilt correction is applied, and CD, LER and LWR can be calculated.

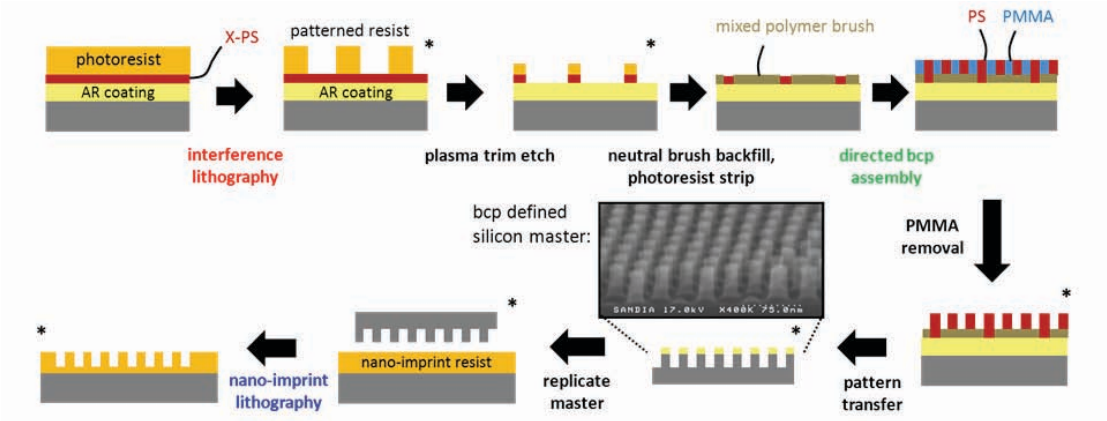

Figure 3.1. Schematic showing process flow from IL patterning through NIL template manufacture. Asterisks indicate non-destructive SEM imaging for process metrology.

Figure 3.2 a.) shows an optical image of a characteristic IL exposure with a grid overlay indicating the region over which data was taken. We chose to study a 1 cm x 2 cm region to get a sense not only of the local variation of parameters, but also the uniformity over a macroscopic region. In this case, SEM images were taken every 2 mm throughout the grid. Figure 3.2 b.) shows a plot of the CD measurement as a function of *x*-*y* coordinates. Over this region, the CD averaged to 42.7 nm with an LER of 4 nm, or 9.4% of the CD.

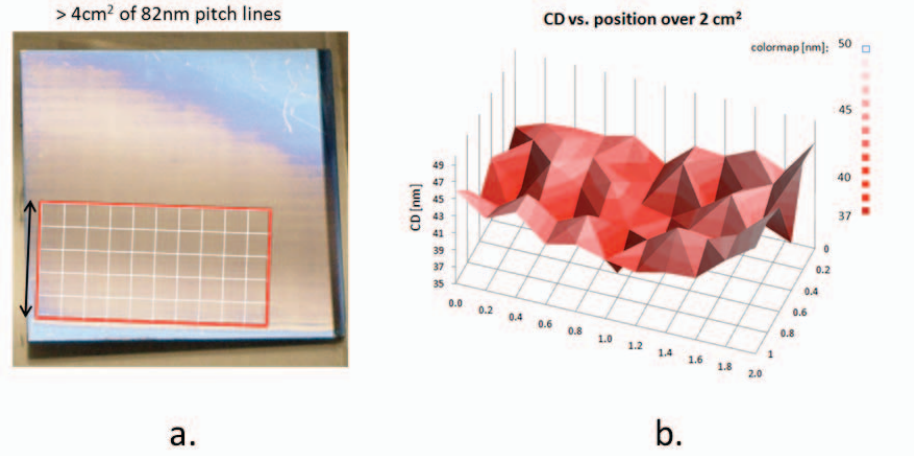

Figure 3.2. a.) Optical image of sample with grid showing location of measurements; b.) Plot of CD over grid.

The next step in the process after the IL exposure is the trim etch step. To study the impact of the trim etch step on CD, LER and LWR, a group of images were taken from the center of the 2 cm^2 region from Figure 3.2 a.). SEM images were taken for a length of 200 μm at 10 μm intervals at which the CD statistics were calculated both before and after the plasma trim etch was performed. Figure 3.3 shows a bar chart comparing the LER before and after the trim etch. After the trim etch process, the CD changed from 43.5 nm to 16.9 nm, while the LER reduced from 4.3 nm to 3.0 nm. Although the absolute LER decreased, the relative LER with respect to the CD has actually increased.

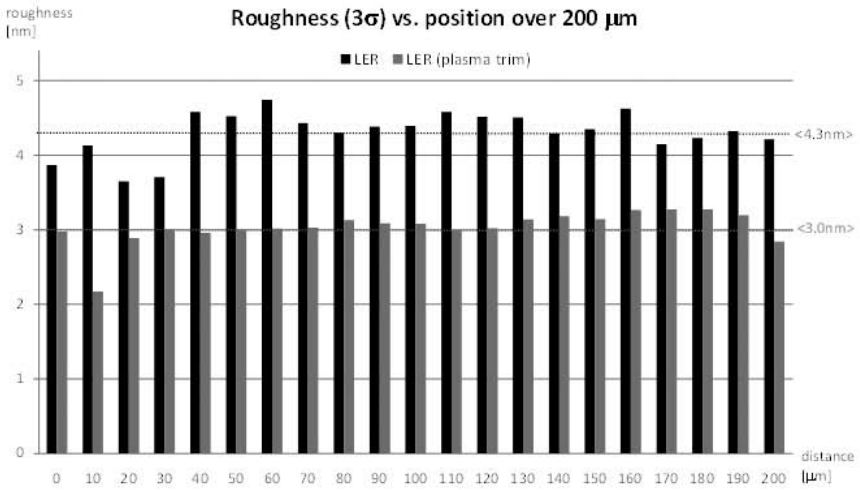

Figure 3.3. Bar chart showing evolution of LER before and after O_2 plasma trim etch.

Finally, DSA was attempted on this sample. Out of the 20 regions sampled in the trim etch study above, DSA was successful in only 4 of the regions, shown in the green region of the bar chart in Figure 3.4, with the corresponding SEMs shown below. For reference, the fingerprint pattern of an unsuccessful DSA region is shown to the right.

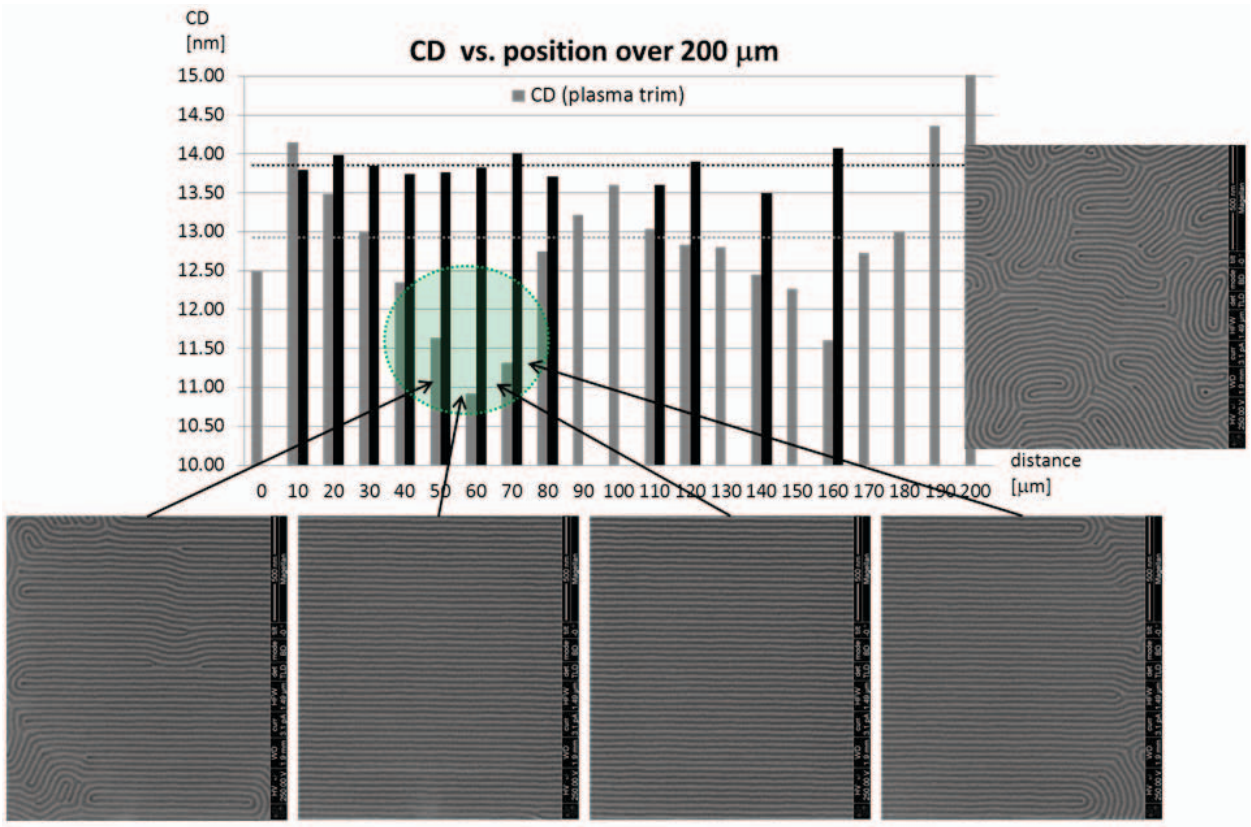

Figure 3.4. Chart and associated SEM images showing the associate of successful DSA with a relatively narrow process window of guiding line spacing on the processed sample.

4. MODELING AND SIMULATION

Block copolymers (BCPs) can self-assemble into complex morphologies, whose structure depends on the characteristics of the blocks. Their ability to self-assemble has led to applications ranging from thermoplastic elastomers to foams and adhesives. More recently, BCPs have received increased attention in the context of nanoscale fabrication, where the objective is to mass-produce precisely ordered nanoscale structures in the 3-50 nm range.[18,19] In a process referred to as BCP lithography, a BCP film is used as a mask for subsequent etching of the underlying substrate. Several strategies have been pursued to achieve long-range order of the BCP mask. These include the application of shear, electric fields, and the use of substrates having a chemical or a topographic pattern.[20-22] For applications in the semiconductor industry, it is essential to create BCP thin films that not only exhibit long-range order, but that are also free of defects over macroscopic areas in excess of 100 cm^2.[23] From an experimental point of view, finding a handful of nanometer scale defects in such large areas can be particularly demanding. We therefore turn to molecular models and statistical mechanical formalisms to determine the probability that distinct defects will arise in ordered BCP thin films.

Defects in BCP thin films assembled on chemically patterned substrates may originate from pattern imperfections, or may be due to kinetic entrapment of imperfect morphologies on a perfect substrate.[5,8,23-26] Several studies have examined the structure and dynamics of defects of BCP thin films on homogeneous surfaces.[27-33] Structural evolution on chemically patterned surfaces, however, is significantly different from that observed on homogeneous substrates.[26] Welander *et al.*, for example, have shown that annealing at elevated temperatures leads to formation of defect-free structures in a matter of minutes.[34] That study was particularly relevant to applications in that it was carried out on stripe-patterned substrates, and with lamellar morphologies that offer potential for device fabrication. A more recent report, using industrial equipment and conditions, has presented a statistical, industrial scale analysis of defects over larger areas than those originally considered by Welander *et al.*, and suggests that it might indeed be possible to obtain defect-free ordered copolymer films over macroscopic areas (with zero dislocation or disclination defects).[35]

Recent work has shown that directed self-assembly (DSA) of diblock copolymer films on chemically patterned substrates can be used to form regular structures (*e.g.*, arrays of lines or dots) and irregular structures (*e.g.*, bends or T-junctions).[23] Perhaps more importantly, DSA on chemical patterns appears to be particularly tolerant to imperfections of the underlying chemical pattern.[5,24] In this work, we have estimated the free energy of commonly observed BCP defects on stripe-patterned substrates and use those estimates to predict the probability that such defects will be observed over macroscopic areas of relevance to applications. The results provide an essential piece of information that has been lacking from discussions of the viability and scalability of BCP assembly for technology applications, namely the equilibrium probability that common defects will be observed over large areas.

As useful and informative as past studies have been, the central questions regarding commonly occurring defects in ordered assemblies of BCPs on patterned substrates remain unanswered. These questions include (i) their actual size, (ii) their free energy and the role of fluctuations on that free energy, (iii) their relative stability, and (iv) the role of substrate patterns

on their formation. We use a coarse grain model[35] to address such questions on three commonly occurring localized defects that are frequently observed in both experiments and simulations of BCPs on stripe-patterned substrates, namely jogs, +1/2 disclinations and edge dislocations.

Molecular simulations also provide insight into both the best choice for the geometry and chemistry of the chemical pattern for DSA, while suggesting the three-dimensional (3D) morphology of block copolymers directed to assemble on the chemical patterns.[36-37] For patterning applications, the best chemical pattern is the one that results in assembled domains that are oriented perpendicular to the substrate, that traverse the thickness of the film, and that form a pattern with a high degree of perfection and a period that matches the pattern period L_s. In previous work with molecular simulations, Detcheverry *et al.*[38] used Monte Carlo simulations of a coarse-grained model to demonstrate the pattern rectification capability of DSA with density multiplication. They showed that for DSA of cylinder-forming block copolymers with 2x density multiplication, the desired structure could be obtained in the film even when the location of the guiding spots in the chemical pattern was randomly varied by as much as 23% of the natural domain spacing. Ruiz *et al.*[5] used similar simulations to compare the effect on DSA of different background and guiding spot affinities for the BCP. They examined four combinations of guiding spot and background affinities (weak-weak, strong-weak, medium- medium, and strong-strong, respectively), and found that the use of a background that was weakly preferential to the matrix block led to the formation of more uniform, perpendicular cylindrical domains, compared to the other two cases. In the case of lamellae-forming block copolymers, Detcheverry *et al.*[8] calculated phase diagrams for DSA with density multiplication for combinations of guiding spot and background affinities for the block copolymer that ranged from (non-preferential)-(non-preferential) to strong-strong. Their simulations revealed that, depending on the pattern line width W as well as the affinity of the chemical pattern stripe and the background with the overlying block copolymer domains (Λ_s and Λ_b, respectively), eight different stable and meta-stable morphologies equilibrated in the presences of the chemical pattern. Structures closest to perpendicular lamellae were obtained when the affinity of the background was relatively weak ($\Lambda_b \leq 0.25$, but not neutral) and $W/L_0 = 0.5$, where L_0 is the bulk period of the block copolymer. The simulations suggest that enhancing the fundamental understanding of the effects of the pattern chemistry and geometry on DSA should provide an opportunity to improve DSA with density multiplication.

In addition to answering fundamental questions about the mechanisms involved in the self-assembly of block copolymer systems, modeling can help answer practical questions which arise in the application of BCP-DSA. For instance, under some circumstances, DSA yields a plan-view pattern that appears to be a highly dense array of cylinders. On cross section, however, it is seen that some of the cylinders do not penetrate all the way through the film. Sidewall profile is another physical variation that can occur in DSA. Sometimes the sidewalls are vertical, while other times they exhibit tapered profiles. Being able to explore this parameter space though simulation offers a massive time savings, along with model-based insight into the mechanisms to describe and control the specific morphologies which emerge from DSA.

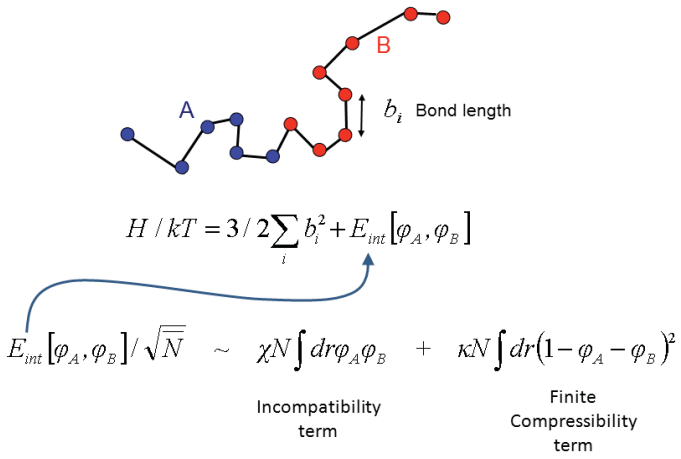

Figure 4.1. Schematic of Gaussian chain modeling of polymer system (top) and Hamiltonian for the discretized system.

Monte Carlo simulations of a course-grained model can provide insight into the assembly behavior of BCP systems. As shown in Figure 4.1, the AB polymer system is modeled as a Gaussian chain discretized into a bead-spring chain. These chains interact via a functional of the local densities. There are two terms in the Hamiltonian, the first term represents energy due to bonds and the second term due to local density, which includes the incompatibility and compressibility terms. In a coarse-grained approach, this system is parameterized by the end to end distance, the number of chains in the volume occupied by a chain, and the number of beads per chain. These models allow for Monte Carlo simulations of systems (typically including 10000 chains), and is efficient enough to consider hundreds of parameter combinations. References X through Y contain details about the models and implementation; references X through Y show how a variety of morphologies can be created by simply varying dimensional parameters of the system and, more importantly, how these simulations have been correlated with experiment. Commonly-observed top-down morphologies and even a variety of cross-section morphologies have been found consistent with simulation; readers are referred to upcoming publications for details.

To reproduce the results in the thin films from experiments, an exponential potential is constructed which has an initial interaction at the surface and then decays over the distance from the surface, while the boundary conditions are periodic in x and y. The interactions can be represented as a sum of pairwise interactions between beads, which allows the calculation of forces for dynamics. Spherical step-like functions are used to determine the interactions, so the beads can be thought of as soft spheres where the pair-wise interaction energy is given by the overlapping volume of the clouds. The Brownian dynamics approach, however, does not conserve momentum. Hydrodynamics plays an important role in the kinetics of microphase separation of hexagonally packed cylinders;[39-40] previous work has shown that dissipative particle dynamics (DPD) reproduces the phase diagram in simple shear. More generally, a variety of reports have highlighted the importance of DPD thermostats in non-equilibrium flows.[41-43] The first step for performing non-equilibrium simulations is implementing simple shear. Using the DPD thermostat and Lees-Edwards boundary conditions is referred to as (DPDT). Interested readers are referred to upcoming publications for explicit details on these efforts.

5. PATTERN TRANSFER

In semiconductor processing, fabrication of a device requires many steps where a desired pattern is created on a substrate. This process is usually composed of two steps: 1) formation of a template pattern in a polymer, and 2) transfer of the soft pattern onto the wafer surface through either additive processes like thin film deposition, or subtractive processes such as dry etching. The semiconductor industry has used photopatterned polymers (photoresist) patterned through optical lithography since its inception. Despite predictions of its demise for many process nodes, the basic steps of depositing a thin film of resist on the device substrate, alignment and registration of the mask image with the current layer on the wafer, exposure and development. As the critical dimensions of the semiconductor device have continued to scale with Moore's law, the process of pattern transfer has also become more difficult. In order to resolve deeply submicron features in the resist, it has become necessary to use thinner resists, which being soft, offer lower resistance to processes such as thin film plasma etching.

The goal of this project was to use interferometric lithography (IL) to chemically pattern a substrate so that block copolymer self-assembly would occur in a directed rather than random fashion. The BCP pattern would then be used to create a NIL mold created by transferring the BCP pattern into the substrate. The pitch of the IL structures used in this work was fixed at either 90 nm or 82 nm. As discussed elsewhere in this report, depending on the dimensions of the IL pattern and the molecular weights of the BCP system, this process can lead to pattern density multiplication. For the molecular weights and viscosities of the BCP used in these experiments, the features can be on the order of 20 nm in diameter. The range of film thickness that yields the preferred BCP pattern is on the order of 30-50 nm. This section of the report details our work toward performing pattern transfer for both IL and BCP patterned structures.

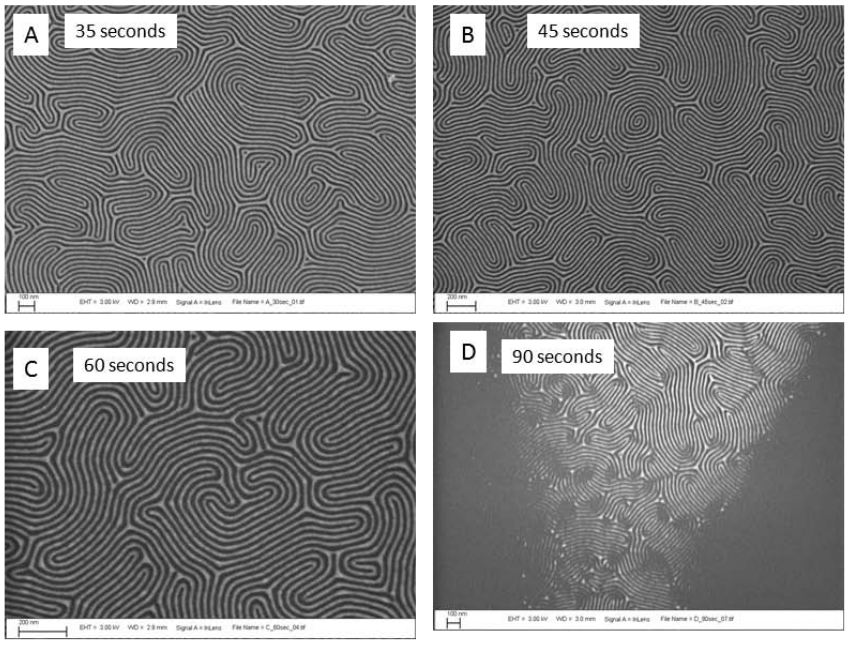

Figure 5.1. Top down SEM images of fingerprint BCP patterns etched in an O_2 plasma for varying lengths of time to selectively remove the PMMA block.

One method for the removal of the PMMA block is to expose the wafer to UV light and then use acetic acid to dissolve out the PMMA block, leaving behind the cross-linked PS block. This approach works with arrays of PMMA cylinders in a PS matrix, because the PS matrix is structurally stable. This approach would not work with 1-D lines because capillary forces upon drying would cause the lines to collapse. For this reason, it is important to develop a dry-etch method to remove the PMMA block. Figure 5.1 contains top-down SEM images of a fingerprint pattern with varying lengths of O_2 plasma etch. These samples were etched in a Plasmatherm RIE with the pressure set at 10 mTorr, O_2 flow at 20 SCCM, forward RF power of 24.3 W and a DC bias of 290V. From these images, clearly 30, 45 and 60 second etches appear to pattern the surface, while 90 seconds is obviously too long. The next step is to determine if the PMMA is removed all the way down to the substrate. Figure 5.2 contains SEM images of cross-sections of the 35, 45 and 60 second etches. Achieving adequate cleaves to reveal good cross-section line profiles was challenging, but from these images, it is apparent that a 35 second etch is sufficient to remove the PMMA block all the way down to the surface.

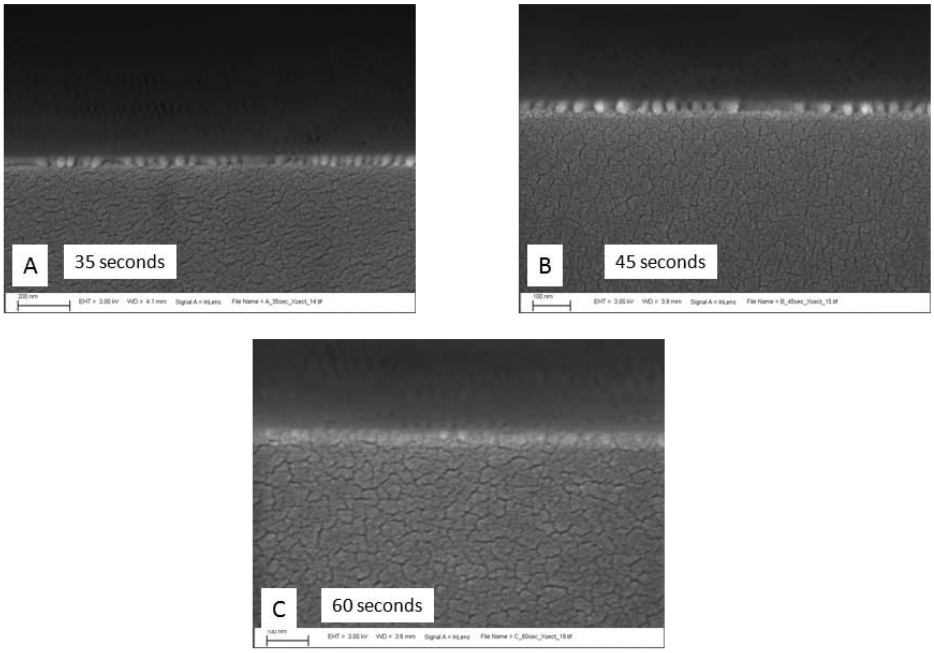

Figure 5.2. Cross-section SEM images of etched patterns to determine if the entire PMMA block was removed.

Once a usable PMMA removal etch was developed, the question was whether this X-PS mask was sufficiently robust to allow pattern transfer into the underlying substrate to create the mask master for NIL. Figure 5.3 contains top-down SEM images of Si_3N_4 coated Si samples. In this case, two different PMMA punch through times were used (30 and 45 seconds) and two Si_3N_4 etch (P: 10mTorr, O_2: 5 SCCMs, CF_4: 45 SCCMs, RF 25W, DC 290) times were used, 30 and 60 seconds. The PS etch mask was removed in an O_2 plasma and the films imaged. From this experiment it is apparent that a 30 second PMMA removal step may not be sufficient given the low contrast for the 30 second nitride etch versus that of the 45 second PMMA removal etch with identical nitride etch conditions in the lower left corner.

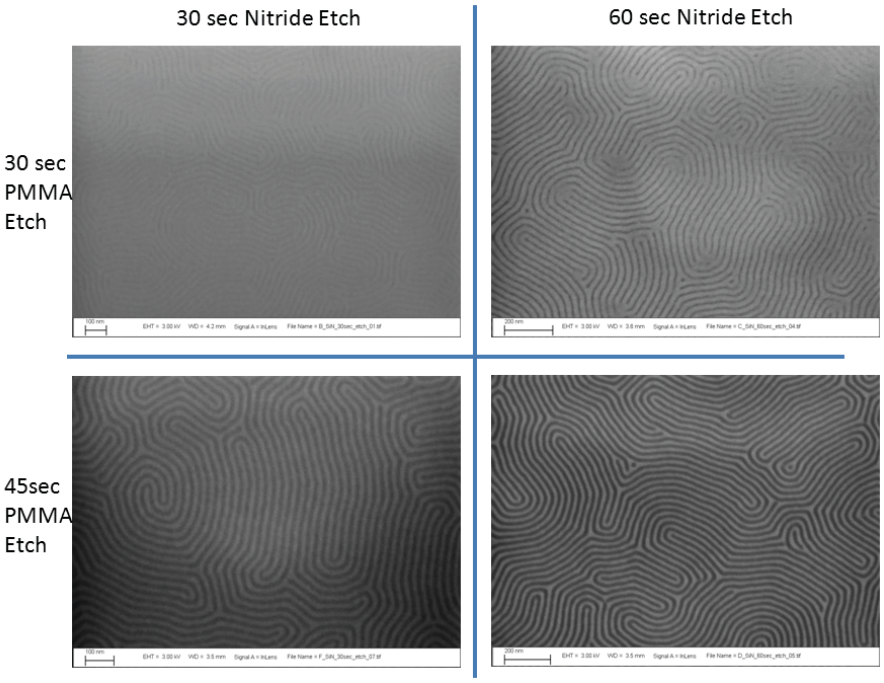

Figure 5.3. Top down SEM images of etched nitride films etched for 30 and 60 seconds, for PMMA block removal etches of 30 and 45 seconds.

Figure 5.4 contains a series of etch times for a silicon wafer with the SiO_2 AR coating. For these wafers a 40 second PMMA etch time was used based on the results from the nitride results above. The SiO_2 etch conditions were: P: 10 mTorr, CHF_3: 45 SCCMs, RF 50W, DC 400V. The cross-sections show that a 60 second etch is sufficient to reach the substrate.

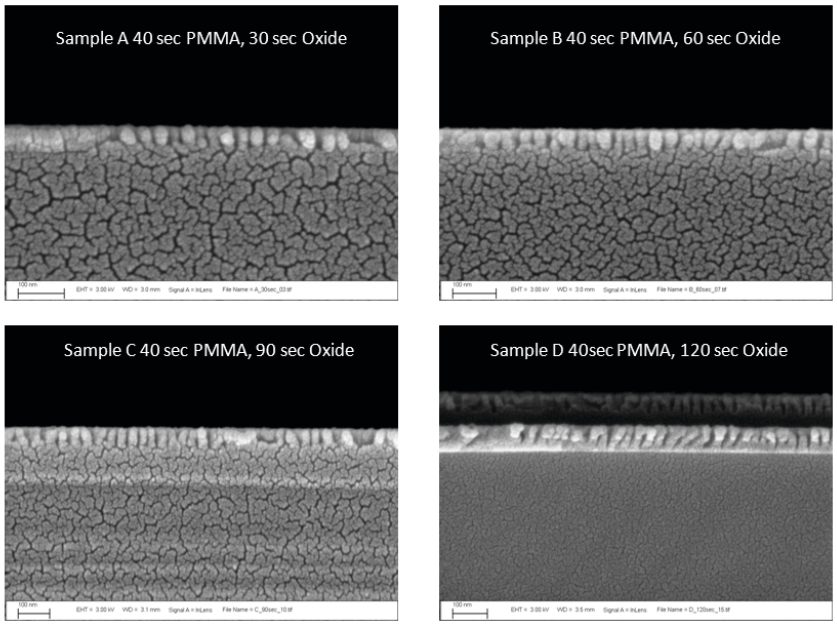

Figure 5.4. Cross-section SEM images of oxide etches using a fingerprint BCP pattern with a 40 sec PMMA removal step and oxide etch.

In addition to the 1-D lamellae patterns above, we also demonstrated etching of 2-D arrays of BCP cylinder patterns. Figure 5.5 contains SEM images of both arrays of holes transferred into the SiO_2 ARC layer on the left and arrays of oxide posts on the right. For the holes, the X-PS BCP mask was used directly as the etch mask, while for the posts, 5 nm of Cr was evaporated onto the sample, and piranha/scotch tape liftoff was performed to remove the Cr coated X-PS mask. The result is an array of Cr dots on the surface of the oxide which served as the etch mask for transferring the pattern into the oxide.

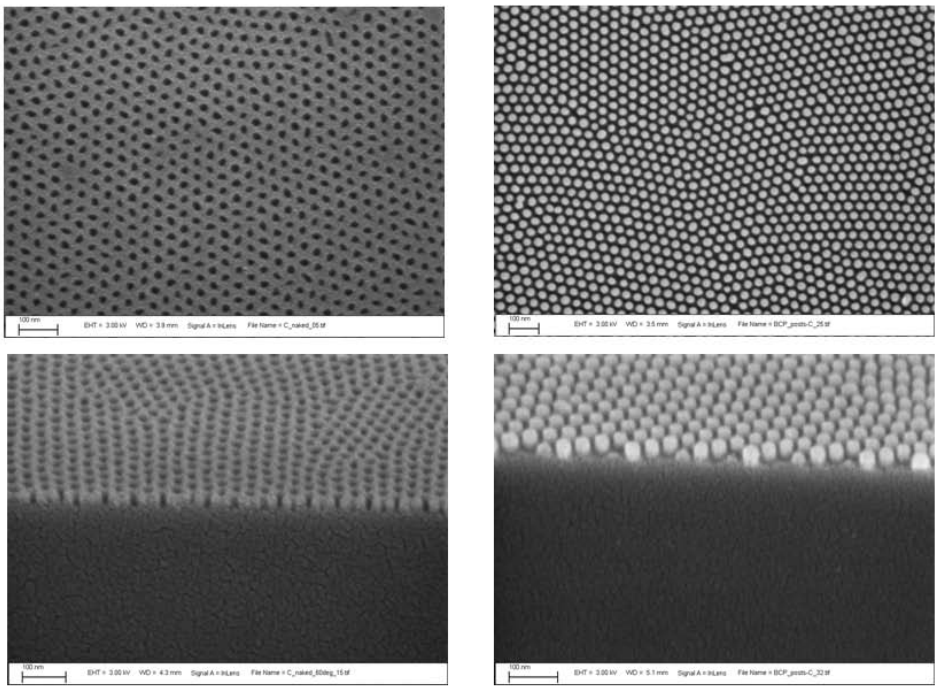

Figure 5.5. Top-down and cross section SEM images of 2-D patterns formed using hexagonal BCP patterns as either an etch or liftoff mask.

6. PROXY APPLICATIONS

6.1 BCP-NIL fabricated SERS platform

Localized surface plasmon resonances are excited when light is incident upon metal nanoparticles, resulting in localized electric field oscillations.[44] Molecules adsorbed to these metal surfaces, and therefore residing within the vicinity of the electric fields, have been shown to exhibit enhanced Raman scattering due to both an increase in light absorption by the molecules as well as an increase in the resulting Raman scattering intensities.[45] This surface enhanced Raman scattering (SERS) phenomenon is well known and was first discovered in the 1970s.[46,47]

When the incident light is near the plasmon resonance frequency of a particular metal material, the effect is more significant. Silver and gold have plasmon resonance frequencies in the visible region and, therefore, are commonly used in performing SERS experiments.[44] The effect can be further enhanced by roughening the metal surfaces or creating shapes with sharp edges or corners to further localize the electric fields, creating "hot spots."[13] Furthermore, placing the particles in close proximity to one another could also enhance the effect by creating collective electric field oscillations.[48,49]

A prototype SERS device was fabricated in the following manner. After the nanoimprint lithography process with a block coplymer template, the residual PMMA layer at the bottom of the holes was removed by an oxygen plasma inductively-coupled reactive ion etch [30 W RF power, 25 SCCM of O_2 flow, and 5 mTorr chamber pressure]. Cr of 1 nm thickness was e-beam evaporated onto the imprinted substrate as an adhesion layer, followed by 5 nm of Au. Lift-off was performed via 30 minutes in an ultrasonic bath to remove the unwanted PMMA and metal layers, leaving behind Au nanodots. It was found that removing 25 nm of the PMMA (half the initial thickness) during the oxygen plasma etch provided optimum conditions for successful resist lift-off. If less than 25 nm of the initial PMMA thickness were etched, the residual PMMA layer from the imprint process was not removed completely. The evaporated metal would, therefore, not adhere to the substrate. If more than 25 nm of the initial PMMA thickness were removed, then lock-in would occur due to excessive sidewall deposition of the evaporated metal. Lift-off would then be unsuccessful in removing the PMMA. Metal thicknesses of 1 nm Cr and 5 nm Au proved to be the most optimal thicknesses for a successful lift-off.

Figure 6.1(a) presents a SEM image of the Cr/Au metal deposited onto the PMMA imprint pattern before lift-off. The metal dots (dark gray) are clearly visible inside the imprinted holes. It is apparent that some dimensionality and circularity have been lost during the nanoimprint pattern transfer process. The imprinted holes now measure 20–35 nm in diameter. After lift-off, Cr/Au nanodots remain on the surface of the silicon substrate. The dimensionality and circularity loss in these nanodots is transferred from the imprint pattern and could be seen in the SEM images in Figures 6.1(b)–6.1(d). The metal nanodots measure 20–33 nm in diameter. Peanut shaped defects are due to the transfer of imperfections from the original block-copolymer assembly, while single dot voids are due to the failure of punching through the entire residual PMMA layer. Atomic force microscopy (AFM) measurements were also performed on the Cr/Au nanodot sample. The height of the nanodots appears relatively uniform across the sample.

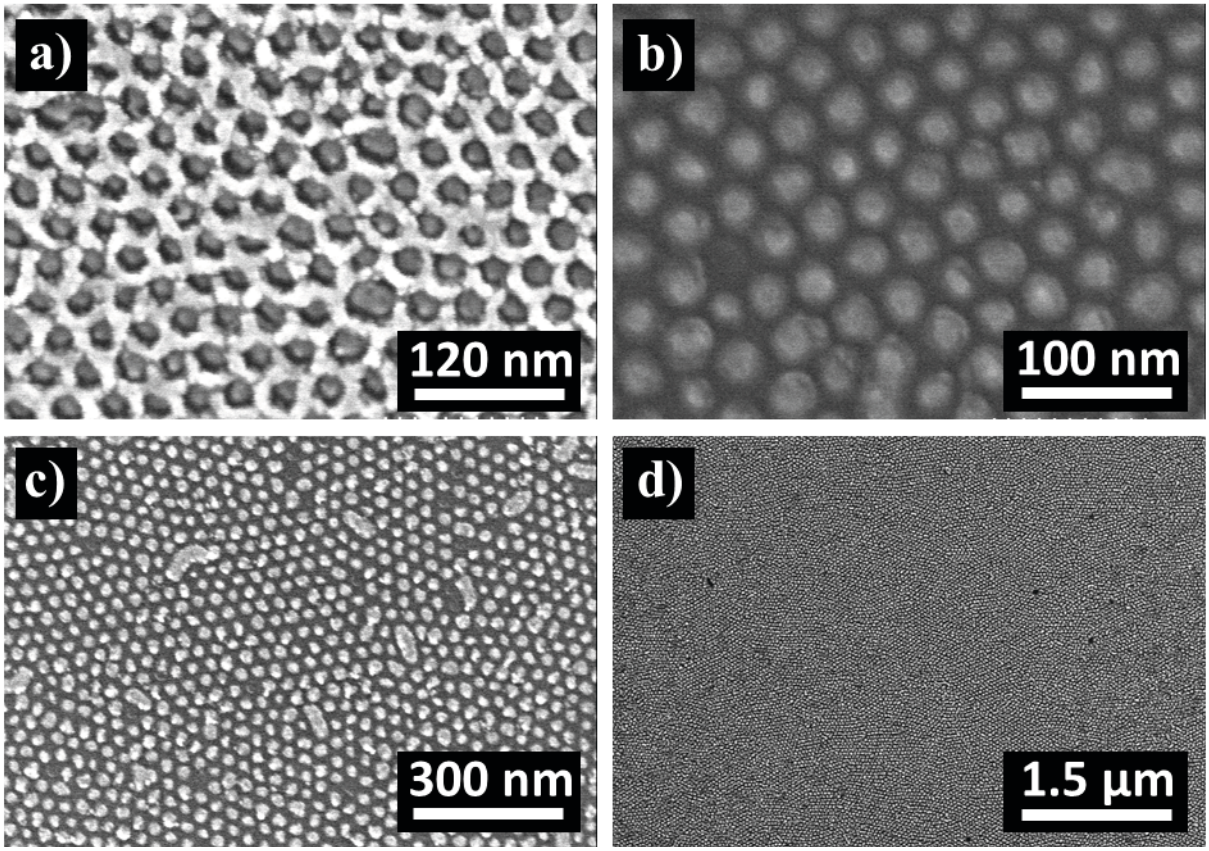

Figure 6.1. Top-down SEM images of the Au nanodot SERS device a) before PMMA photoresist lift-off and b) – d) after lift-off (figure reprinted with permission from the American Vacuum Society).[50]

R6G was chosen as the interrogation molecule for testing the SERS device due to its richly featured and recognizable Raman scattering spectrum.[16] One droplet (approximately 0.05 ml) of $1x10^{5}M$ R6G in methanol was placed on a 1x1 cm^2 device chip (cleaved from the original wafer) and allowed to air dry. The 532 nm line of a neodymium:yttrium aluminum garnet laser was used as the excitation source. Gold was chosen as the plasmonic material due to its well-known resonance in the mid-visible region and was, therefore, well matched to the excitation wavelength.[44,45] The total power incident on the substrate surface was approximately 1 mW and the laser spot size was approximately 650 nm in diameter. The Raman scattering spectra were collected over 1-second collection times.

The Raman scattering spectra in Figure 6.2 indicate an enhancement of the R6G peaks in the presence of the Au nanodots. The spectra were collected in three scenarios: (1) the laser spot was focused on an area of the device chip where there are Au nanodots, (2) the laser spot was focused on a bare silicon area of the same device chip where there were no Au nanodots, and (3) the laser spot was focused on a control chip of bare silicon with no Au nanodots.

In scenario 1, many peaks are visible in the Raman scattering spectra. The peaks denoted by the arrows are associated with R6G and are clearly visible.[16] In scenarios 2 and 3, the same peaks are not discernible, suggesting enhanced Raman scattering in scenario 1. Furthermore, the

519 cm^{-1} peak is clearly visible on all three spectra and is associated with the Raman signature of the silicon substrate. In fact, the magnitude of the 519 cm^{-1} peaks in the three scenarios is virtually unchanged, which supports the conclusion that the enhancement in the R6G peaks is indeed caused by the presence of the Cr/Au nanodots. Scenario 2 further supports the claim by ensuring that approximately the same number of R6G molecules resided in the interrogation areas, since the substrate used in scenarios 1 and 2 was the same substrate that was subjected to the same droplet of R6G solution. In total, approximately 15 measurements were done on independently located Au nanodots to verify the enhancement.

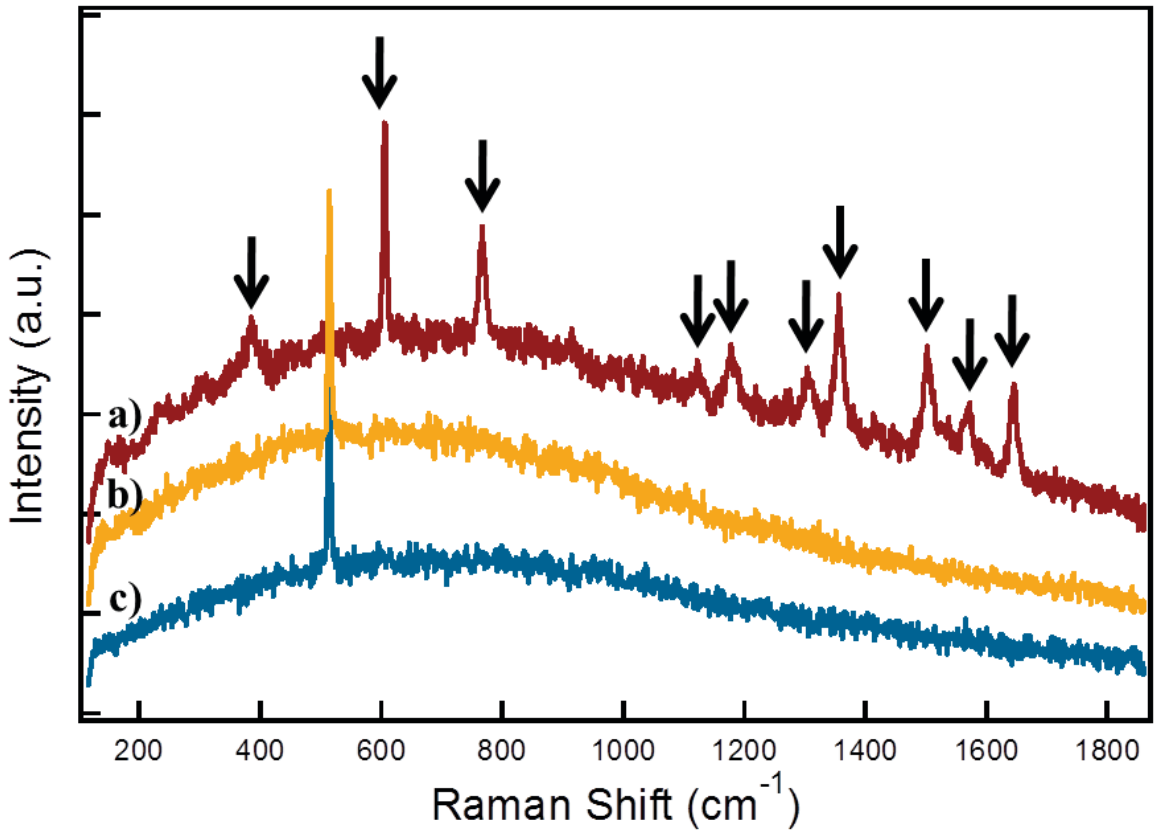

Figure 6.2. Raman scattering plots of R6G on a) device chip: patterned section, b) control chip: bare silicon, and c) device chip: bare silicon section. Black arrows denote R6G scattering peaks (figure reprinted with permission from the American Vacuum Society).[50]

In summary, the integration of diblock-copolymer self-assembly and nanoimprint lithography presents a more rapid and cost-effective approach to nanofabrication as compared to conventional e-beam template writing. The technique enables sub-50 nm feature pattern transfers. We have demonstrated the fabrication of a Cr/Au nanodot SERS device and confirmed the enhanced Raman scattering signals of R6G molecules adsorbed onto the device surface.

Initial results show varying defects and imperfections that resulted from each pattern transfer step. Future work will focus on obtaining more ordered diblock-copolymer assemblies, improving imprint yield over larger areas, eliminating imprint voids, and retaining the

dimensionality and fidelity of shapes. Also, the magnitude of enhancement of Raman scattering peaks could likely be improved by optimizing the size of the nanoparticles.

6.2 UV Wire Grid Polarizer

Controlling the polarization state of light is very important for many applications in optics and electromagnetics. In long wavelength applications, wire grid polarizers (WGP) are used to great effect to allow linearly polarized light of one polarization to pass, while blocking the orthogonal polarization. WGPs work by allowing electrons in the metal lines (wires) to oscillate in response to incident light. The oscillating electrons create a field that cancels the field from the incident light, so that the portion of incident light polarized along the wires is removed from the transmitted light. In order for a WGP to function, the spacing of the wires must be significantly smaller than the incident wavelength – a condition which is easy to achieve at RF and microwave frequencies, but much more difficult for shorter wavelengths. In this proxy application, we demonstrate WGP behavior for optical frequencies using just standard IL lithography. The processing steps we use are fully consistent with an implementation with IL directed density multiplied DSA-BCP and NIL fabrication.

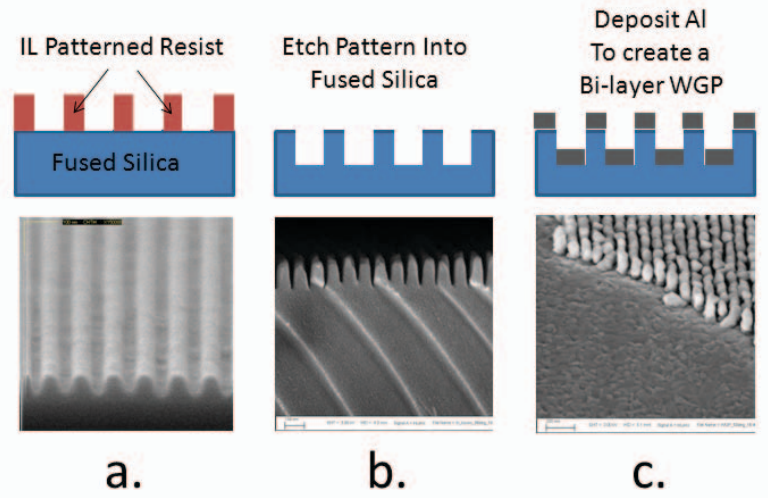

Figure 6.4. Schematic (top) and actual SEM cross-section images (bottom) of WGP processing steps.

Figure 6.4 shows a schematic view of the process outline in the top row for a bi-layer WGP, with corresponding SEM images of the steps in the bottom row. Starting from the IL patterned resist in the first pane, it is apparent that the achieving high grating contrast would be challenging. Indeed, upon pattern transfer, the SEM cross-section image in the middle pane shows significant rounding and a line/space ratio that is significantly higher than 0.5. Finally, the Al evaporation followed the underlying topology with the addition of significant wetting issues resulting in a highly granular Al deposition.

Figure 6.5a.) shows the results of modeling on the extinction ratio of bi-layer wire grid polarizers using measured material parameters. The graph on the right shows the measured WGP for the sample shown in Figure 6.4, measured using a VASE instrument. It is apparent that even though the microscopic structure of the WGP sample is sub-optimal, we are still able to achieve

extinction ratios between the allowed/rejected polarization of >100 from the mid-UV (300 nm) out through the visible, demonstrating the potential of this approach.

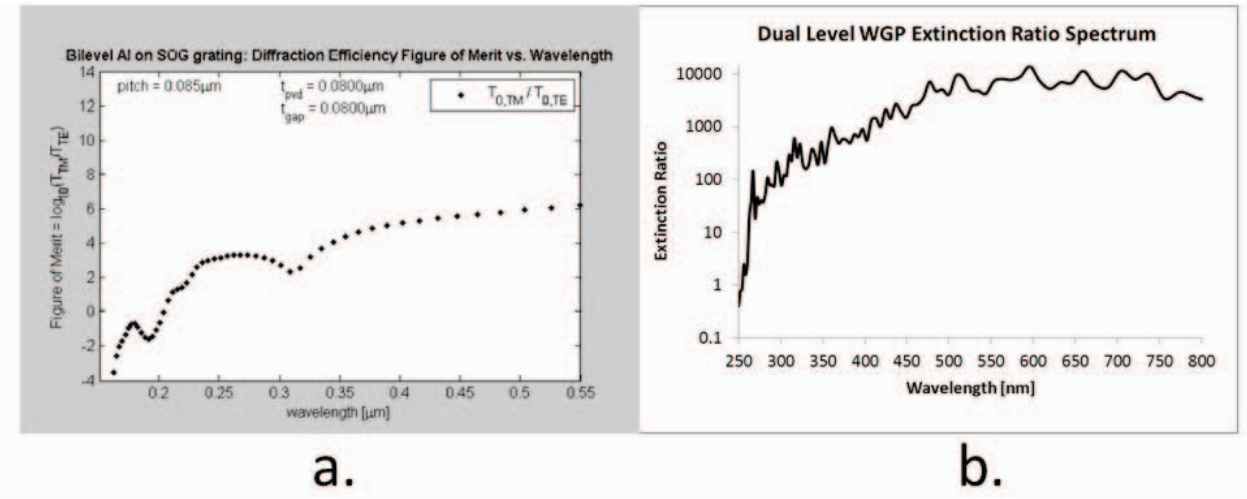

Figure 6.5. a.) plot of log of the modeled extinction ratio for a bi-level WGP; b.) measured extinction ratio for WGP samples.

7. CONCLUSIONS

This program began with a grand vision of melding three next generation lithography technologies into a seamless über-lithography technique, and furthermore quantifying specific process parameters such as CD, LER, and LWR evolution at each step. Given the footprint of the program (~1 student per collaborator) and the relative difficulty of successfully implementing each of the component technologies, we were unable to consistently run the anticipated process flow. Nevertheless, we were able to demonstrate examples of IL-to-BCP directed assembly, BCP-to-NIL master pattern formation, and IL-NIL master pattern formation. In addition, we were able to perform singlet instances of the process flow, and were able to quantify the evolution of the statistical process parameters for that case. A true analysis yielding valuable statistical process control data would require many fabrication/metrology cycles.

Another source of delay involved imaging the samples. Fabrication on these size scales and quantification of the process steps absolutely requires high resolution imaging, and in the case of in-situ monitoring, the samples cannot be coated. Even in cases where coating the samples is allowed, cleaving delicate polymer patterns with 20nm features on insulating fused silica substrates is challenging. In a future effort aimed at this same topic, incorporating a dedicated metrology SEM would be beneficial.

8. REFERENCES

1. International Technology Roadmap for Semiconductors, 2009 Edition, Lithography (2009); Reports are available at: www.itrs.net

2. Lithography ITWG Report (chairmen: M. Vasconi, J.-W. Gemmink, M. Sasago, H. Ohtsuka, H.K. Cho, K.S. Shin, T. Yen, Y.C. Ku, H. Levinson, and G. Gomba), ITRS Conference, November 29, 2001. Santa Clara, CA (2011); available at www.itrs.net

3. Michael D. Austin, Haixiong Ge, Wei Wu, Mingtao Li, Zhaoning Yu, D. Wasserman, S. A. Lyon, and Stephen Y. Chou, "Fabrication of 5 nm linewidth and 14 nm pitch features by nanoimprint lithography," *Appl. Phys. Lett.*, **84** 5299 (2004).

4 J.Y. Cheng, C.T. Rettner, D.P. Sanders, H.-C. Kim, and W.D. Hinsberg, "Dense Self-Assembly on Sparse Chemical Patterns: Rectifying and Multiplying Lithographic Patterns Using Block Copolymers" *Advanced Materials*, **20**[16] 3155-3158 (2008).

5. R. Ruiz, H. Kang, F.A. Detcheverry, E. Dobisz, D.S. Kercher, T.R. Albrecht, J.J. de Pablo, and P.F. Nealey, "Density Multiplication and Improved Lithography by Directed Block Copolymer Assembly," *Science*, **321** 936-939 (2008).

6. M.P. Stoykovich, K.C. Daoulas, M. Müller, H.M. Kang, J.J. de Pablo, and P.F. Nealey, "Remediation of Line Edge Roughness in Chemical Nanopatterns by the Directed Assembly of Overlying Block Copolymer Films," *Macromolecules*, **43**[5] 2334-2342 (2010).

7. D. Xia, Z. Ku, S.C. Lee, and S.R.J. Brueck, "Nanostructures and Functional Materials Fabricated by Interferometric Lithography," *Advanced Materials*, **23**[2] 147-179 (2011).

8. F.A. Detcheverry, G. Liu, P.F. Nealey, and J.J. de Pablo, "Interpolation in the Directed Assembly of Block Copolymers on Nanopatterned Substrates: Simulation and Experiments", *Macromolecules*, **43**[7] 3446-3454 (2010).

9. E.W. Edwards, M.F. Montague, H.H. Solak, C.J. Hawker, and P.F. Nealey, "Precise Control over Molecular Dimensions of Block-Copolymer Domains Using the Interfacial Eenergy of Chemically Nanopatterned Substrates," *Advanced Materials*, **16**[15] 1315-1319 (2004).

10. C.-C. Liu, P.F. Nealey, A.K. Raub, P.J. Hakeem, S.R.J. Brueck, E. Han, and P. Gopalan, "Integration of block copolymer directed assembly with 193 immersion lithography," *Journal of Vacuum Science and Technology B*, **28** C6B30 (2010).

11. S.Y. Chou, P.R. Krauss, and P.J. Renstrom, "Nanoimprint Lithography," *Journal of Vacuum Science and Technology B*, **14**[6] 4129-4133 (1996).

12. H. Tan, L. Kong, M. Li, C. Steere, and L. Koecher, "Current status of Nanonex nanoimprint solutions," *Proceedings of the SPIE*, **5374**[1] 213-221 (2004).

13. M.J. Mulvihill, X.Y. Ling, J. Henzie, and P.Yang, "Anisotropic Etching of Silver Nanoparticles for Plasmonic Structures capable of Single-Particle SERS," *J. Am. Chem. Soc.*, **132** 268-274 (2010).

14. M.A. Noginov, M. Vondrova, S.N. Williams, M. Bahoura, V.I. Gavrilenko, S.M. Black, V.P. Drachev, V.M. Shalaev, and A. Sykes, "Spectroscopic Studies of Liquid Solutions of R6G Laser Dye and Ag Nanoparticle Aggregates," *J. Opt. A: Pure Appl. Opt.*, **7** S219-S229 (2005).

15. J. Chen, T. Martensson, K. A. Dick, K. Deppert, H.Q. Xu, L. Samuelson, and H. Xu, "Surface-Enhanced Raman Scattering of Rhodamine 6G on Nanowire Arrays Decorated with Gold Nanoparticles," *Nanotechnology*, **19** 275712 (2008).

16. A.M. Michaels, M. Nirmal, and L.E. Brus, "Surface Enhanced Raman Spectroscopy of Individual Rhodamine 6G Molecules on Large Ag Nanocrystals," *J. Am. Chem. Soc.*, **121** 9932-9939 (1999).

17. J. Canny, "A Computational Approach to Edge Detection," IEEE Transactions on Pattern Analysis and Machine Intelligence, **PAMI-8**[6] 679-698 (1986).

18. F. Bates and G. Fredrickson, "Block Copolymers - Designer Soft Materials," Physics Today **52** 32 (1999).

19. M. Park, C. Harrison, P.M. Chaikin, R.A. Register, and D.H. Adamson, "Block Copolymer Lithography: Periodic Arrays of ~10^{11} Holes in 1 Square Centimeter," *Science*, **276** 1401-1401 (1997).

20. M. Lazzari, G. Liu, and S. Lecommandoux, Block Copolymers in Nanoscience, Vol. 1 (Wiley-VCH Weinheim, 2006).

21. S. Park, D.H. Lee, J. Xu, B. Kim, S.W. Hong, U. Jeong, T. Xu, and T.P. Russell, "Macroscopic 10-Terabit-per-Square-Inch Arrays from Block Copolymers with Lateral Order," *Science*, **323** 1030-1033 (2009).

22. I. Bita, J.K.W. Yang, Y.S. Jung, C.A. Ross, E.L. Thomas, and K.K. Berggren, "Graphoepitaxy of Self-Assembled Block Copolymers on Two-Dimensional Periodic Patterned Templates," *Science*, **321** 939-943 (2008).

23. M.P. Stoykovich, H. Kang, K.Ch. Daoulas, G. Liu, C.-C. Liu, J.J. de Pablo, M. Müller, and P.F. Nealey, "Directed Self-Assembly of Block Copolymers for Nanolithography: Fabrication of Isolated Features and Essential Integrated Circuit Geometries," *ACS Nano*, **1**[3] 168-175 (2007).

24. E.W. Edwards, M. Müller, M.P. Stoykovich, H.H. Solak, J.J. de Pablo, and P.F. Nealey, "Dimensions and Shapes of Block Copolymer Domains Assembled on Lithographically Defined Chemically Patterned Substrates," *Macromolecules,* **40**[1] 90-96 (2007).

25. F. Detcheverry, G. Liu, P.F. Nealey, and J.J. de Pablo, “Interpolation in the Directed Assembly of Block Copolymers on Nanopatterned Substrates: Simulation and Experiments,” *Macromolecules*, **43**[7] 3446-3454 (2010).

26. E.W. Edwards, M.P. Stoykovich, M. Müller, H.H. Solak, J.J de Pablo, and P.F. Nealey, “Mechanism and Kinetics of Ordering in Diblock Copolymer Thin Films on Chemically Nanopatterned Substrates,” *J. Polymer Sci. B: Polymer Physics*, **43** 3444-3459 (2005).

27. J. Hahm, W.A. Lozes, H.M. Jaeger, and S.J. Sibener, “Defect evolution in ultrathin films of polystyrene-block-polymethylmethacrylate diblock copolymers observed by atomic force microscopy,” *J. Chem. Phys.*, **109** 10111 (1998).

28. C. Harrison, Z. Cheng, S. Sethuraman, D.A. Huse, P.M. Chalkin, D.A. Vega, J.M. Sebastian, R.A. Register, and D.H. Adamson, “Dynamics of pattern coarsening in a two-dimensional smectic system,” *Phys. Rev. E*, **66** 011706 (2002).

29. C. Harrison, D.H. Adamson, Z. Cheng, J.M. Sebastian, S. Sethuraman, D.A. Huse, R.A. Register, and P.M. Chailkin, “Mechanisms of Ordering in Striped Patternes,” *Science*, **290**[5496] 1558-1560 (2000).

30. R. Segalman, K.E. Schaffer, G.H. Fredrickson, E.J. Kramer, and S. Magonov, “Topographic Templating of Islands and Holes in Highly Asymmetric Block Copolymer Films,” *Macromolecules*, **36**[12] 4498-4506 (2003).

31. L.L. Tsarkova, A.A. Horvat, G.G. Krausch, A.V. Zvelindovsky, G.J. Agur, GJ Sevink, and R.R. Magerle, “Defect evolution in block copolymer thin films via temporal phase transitions,” *Langmuir*, **22**[19] 8089-8095 (2006).

32. A. Horvat, G.J. Agur Sevink, A.V. Zvelindovsky, A. Krekhov, and L. Tsarkova, “Specific features of defect structure and dynamics in the cylinder phase of block copolymers,” *ACS Nano*, **2**[6] 1143-1152 (2008).

33. A.W. Bosse, S.W. Sides, K. Katsov, C.J. Garcia-Cervera, and G.H. Fredrickson, “Defects and Their Removal in Block Copolymer Thin Film Simulations,” J. Polym. Sci. B: Polym. Phys., **44** 2495 (2006).

34. A. M. Welander, K. O., H. Kang, H. H. Solak, M. Müller, J. J. de Pablo, and P. F. Nealey, “Rapid directed assembly of block copolymer films at elevated temperatures,” *Macromolecules*, **41**[8] 2759-2761 (2008).

35. C. Bencher, J. Smith, L. Miao, C. Cai, Y. Chen, J.Y. Cheng, D.P. Sanders, M. Tjio, H.D. Truong, S. Holmes, and W.D. Hinsberg, “Self-assembly patterning for sub-15nm half-pitch: a transition from lab to fab,” *Proc. SPIE*, **7970** 79700F (2011).

36. F.A. Detcheverry, D.Q. Pike, U. Nagpal, P.F. Nealey, and J.J. de Pablo, "Theoretically informed coarse grain simulations of block copolymer melts: method and applications," *Soft Matter*, **5** 4858 (2009).

37. Q. Wang, S.K. Nath, M.D. Graham, P.F. Nealey, and J.J. de Pablo, "Symmetric diblock copolymer thin films confined between homogeneous and patterned surfaces: Simulations and theory," *J. Chem. Phys.*, **112** 9996-10010 (2000).

38. F.A. Detcheverry, P.F. Nealey, and J.J. de Pablo, "Directed Assembly of a Cylinder-Forming Diblock Copolymer: Topographic and Chemical Patterns," *Macromolecules*, **43**[15] 6495-6504 (2010).

39. R.D. Groot, T.J. Madden, and D.J. Tildesley, "On the role of hydrodynamic interactions in block copolymer microphase separation," *J. Chem. Phys.*, **110** 9739 (1999).

40. R.D. Groot and T.J. Madden, "Dynamic simulation of diblock copolymer microphase separation," *J. Chem. Phys.*, **108** 8713 (1998).

41. C. Pastorino, T. Kreer, M. Müller, and K. Binder, "Comparison of dissipative particle dynamics and langevin thermostats for out-of-equilibrium simulations of polymeric systems," *Phys. Rev. E*, **76[**2] 026706 (2007).

42. H. Guo, K. Kremer, and T. Soddemann, "Nonequilibrium molecular dynamics simulation of shear-induced alignment of amphiphilic model systems," *Phys. Rev. E*, **66[**6] 061503 (2002).

43. H. Guo, "Shear-induced parallel-to-perpendicular orientation transition in the amphiphilic lamellar phase: A nonequilibrium molecular-dynamics simulation study," *J. Chem. Phys.*, **124** 054902 (2006).

44. W.A. Murray and W.L. Barnes, "Plasmonic Materials," *Adv. Mater.*, **19** 3771-3782 (2007).

45. K. Okamoto, I. Niki, A. Shvartser, Y. Narukawa, T. Mukai, and A. Scherer, "Surface-plasmon-enhanced light emitters based on InGaN quantum wells," *Nature Mater.*, **3** 601-605 (2004).

46. M. Fleischmann, P.J. Hendra, and A.J. McQuillan, "Raman Spectra of Pyridine Adsorbed at a Silver Electrode," *Chem. Phys. Lett.*, **26**[2] 163-166 (1974).

47. D.L. Jeanmaire and R.P. Van Duyne, "Surface Raman Spectroelectrochemistry: Part 1. Heterocyclic, Aromatic, and Aliphatic Amines Adsorbed on the Anodized Silver Electrode," *J. Electroanal. Chem.*, **84** 1-20 (1977).

48. M.A. Noginov, M. Vondrova, S.N. Williams, M. Bahoura, V.I. Gavrilenko, S.M. Black, V.P. Drachev, V.M. Shalaev, and A. Sykes, "Spectroscopic Studies of Liquid Solutions of

R6G Laser Dye and Ag Nanoparticle Aggregates," *J. Opt. A: Pure Appl. Opt.*, **7** S219-S229 (2005).

49. J. Chen, T. Martensson, K.A. Dick, K. Deppert, H.Q. Xu, L. Samuelson, and H. Xu, "Surface-Enhanced Raman Scattering of Rhodamine 6G on Nanowire Arrays Decorated with Gold Nanoparticles," *Nanotechnology*, **19** 275712 (2008).

50. E.L. Yang, C.-C. Liu, C.Y.P. Yang, C.A. Steinhaus, P.F. Nealey, and J.L. Skinner, "Nanofabrication of SERS device by an integrated block-copolymer and nanoimprint lithography method," *J. Vac. Sci. Tech. B*, **28** C6M93 (2010).

51. J. Homola, "Surface Plasmon Resonance Sensors for Detection of Chemical and Biological Species," *Chem. Rev.*, **108**[2] 462-493 (2008).

52. D. Pacifici, H. J. Lezec, and H. A. Atwater, "All-optical modulation by plasmonic excitation of CdSe quantum dots," *Nat. Photon.*, **1** 402-406 (2007).

53. J. L. Skinner, A. A. Talin, and D. A. Horsley, "A MEMS light modulator based on diffractive nanohole gratings," *Opt. Express,* **16**[6] 3701-3711 (2008).

54. J. L. Skinner, L. L. Hunter, A. A. Talin, J. Provine, and D. A. Horsley, ""Large-area subwavelength aperture arrays fabricated using nanoimprint lithography," *IEEE T. Nanotechnol.*, **7**[5] 527-531 (2008).

55. H. F. Ghaemi, T. Thio, D. E. Grupp, T. W. Ebbesen, and H. J. Lezec, "Surface plasmons enhance optical transmission through subwavelength holes," *Phys. Rev. B*, **58**[11] 6779-6782 (1998).

56. T. Thio, H.F. Ghaemi, H.J. Lezec, P.A. Wolff, and T.W. Ebbesen, "Surface-plasmon-enhanced transmission through hole arrays in Cr films," *J. Opt. Soc. Am. B,* **16**[10] 1743-1748 (1999).

57. W. L. Barnes, A. Dereux, and T. W. Ebbesen, "Surface plasmon subwavelength optics," *Nature*, **424** 824-830 (2003).

58. L. Martin-Moreno, F.J. Garcia-Vidal, H.J. Lezec, K.M. Pellerin, T. Thio, J.B. Pendry, and T.W. Ebbesen, "Theory of Extraordinary Optical Transmission through Subwavelength Hole Arrays," *Phys. Rev. Lett.*, **86**[6] 1114-1117 (2001).

59. K.L. van der Molen, F.B. Segerink, N.F. van Hulst, and L. Kuipers, "Influence of hole size on the extraordinary transmission through subwavelength hole arrays," *Appl. Phys. Lett.*, **85**[19] 4316-4318 (2004).

60. M.M. Miller and A.A. Lazarides, "Sensitivity of Metal Nanoparticle Surface Plasmon Resonance to the Dielectric Environment," *J. Phys. Chem. B*, **109**[46] 21556-21565 (2005).

61. E. Hutter and J.H. Fendler, "Exploitation of Localized Surface Plasmon Resonance," *Adv. Mater.*, **16**[19] 1685-1706 (2004).

62. T.R. Jensen, M.D. Malinsky, C.L. Haynes, and R.P. Van Duyne, "Nanosphere Lithography: Tunable Localized Surface Plasmon Resonance Spectra of Silver Nanoparticles," *J. Phys. Chem. B*, **104** 10549-10556 (2000).

63. Y.G. Sun and Y.N. Xia, "Synthesis and characterization of metal nanostructures with hollow interiors," *Proc. SPIE*, **5221** 164-173 (2003).

64. K.M. Byun, M.L. Shuler, S.J. Kim, S.J. Yoon, and D. Kim, "Sensitivity Enhancement of Surface Plasmon Resonance Imaging Using Periodic Metallic Nanowires," *J. Lightwave Technol.* **26**[11] 1472-1478 (2008).

65. L. Gunnarsson, E.J. Bjerneld, H. Xu, S. Petronis, B. Kasemo, and M. Kall, "Interparticle coupling effects in nanofabricated substrates for surface-enhanced Raman scattering," *Appl. Phys. Lett.*, **78** 802-804 (2001).

66. N. Felidj, S.L. Truong, J. Aubard, G. Levi, J.R. Krenn, A. Hohenau, A. Leitner, and F.R. Aussenegg, "Gold particle interaction in regular arrays probed by surface enhanced Raman scattering," *J. Chem. Phys.*, **120** 7141-7146 (2004).

67. W.C. Lin, L.S. Liao, Y.H. Chen, H.C. Chang, D.P. Tsai, and H.P. Chiang, "Size Dependence of Nanoparticle-SERS Enhancement from Silver Film over Nanosphere (AgFON) Substrate," *Plasmonics*, **6**[2] 201-206 (2011).

68. L.A. Lyon, D.J. Pena, and M.J. Natan, "Surface Plasmon Resonance of Au Colloid-Modified Au Films: Particle Size Dependence," *J. Phys. Chem. B*, **103**[28] 5826-5831 (1999).

69. H. Wang, C.S. Levin, and N.J. Halas, "Nanosphere Arrays with Controlled Sub-10-nm Gaps as Surface-Enhanced Raman Spectroscopy Substrates," *J. Am. Chem. Soc.*, **127**[43] 14992-14993 (2005).

70. C.L Haynes, A.D. McFarland, and R.P. Duyne, "Surface-Enhanced Raman Spectroscopy," *Anal. Chem.*, **77**[17] 338A-346A (2005).

71. A. Campion and P. Kambhampati, "Surface-enhanced Raman scattering," *Chem. Soc. Rev.* **27**[4] 241-250 (1998).

72. M. Kahraman, N. Tokman, and M. Culha, "Silver Nanoparticle Thin Films with Nanocavities for Surface-Enhanced Raman Scattering," *Chem. Phys. Chem.* **9**[6] 902-910 (2008).

73. W.B. Cai, B. Ren, X.Q. Li, C.X. She, F.M. Liu, X.W. Cai, and Z.Q. Tian, "Investigation of surface-enhanced Raman scattering from platinum electrodes using a confocal Raman

microscope: dependence of surface roughening pretreatment," *Surf. Sci.*, **406**[1-3] 9-22 (1998).

74. A.M. Schwartzberg, C.D. Grant, A. Wolcott, C.E. Talley, T.R. Huser, R. Bogomolni, and J.Z. Zhang, "Unique Gold Nanoparticle Aggregates as a Highly Active Surface-Enhanced Raman Scattering Substrate," *J. Phys. Chem. B*, **108**[50] 19191-19197 (2004).

75. R. Gupta and W.A. Weimer, "High enhancement factor gold films for surface enhanced Raman spectroscopy," *Chem. Phys. Lett.*, **374**[2-4] 302-306 (2003).

76. L. Maya, C.E. Vallet, and Y.H. Lee, "Sputtered gold films for surface-enhanced Raman scattering," *J. Vac. Sci. Technol. A*, **15** 238-242 (1997).

77. F. Przybilla, A. Degiron, J.Y. Laluet, C. Genet, and T.W. Ebbesen, "Optical transmission in perforated noble and transition metal films," *J. Opt. A-Pure Appl. Op.*, **8**[5] 458-463 (2006).

78. J.J. Wang, J. Deng, X. Deng, F. Liu, P. Sciortino, L. Chen, A. Nikolov, and A. Graham, "Innovative High Performance Nanowire-Grid Polarizers and Integrated Isolators," *IEEE J. Sel. Topics in Quant. Electron.*, **11** 241-253 (2005).

79. X. Liu, X. Deng, P. Sciortino, M. Buonanno, F. Walters, R. Varghese, J. Bacon, L. Chen, N. O'Brien, and J.J. Wang, "Large-Area, 38 nm Half-Pitch Grating Fabrication by Using Atomic Spacer Lithography from Aluminum Wire Grids," *Nano Lett.*, **6**[12] 2723-2727 (2006).

80. V. Pelletier, K. Asakawa, M. Wu, D.H. Adamson, R.A. Register, and P.M. Chaikin, "Aluminum nanowire polarizing grids: Fabrication and Analysis," *Appl. Phys. Lett.*, **88** 211114 (2006).

81. Y. Ekinci, H.K. Solak, C. David, and H. Sigg, "Bilayer Al wire-grids as broadband and high performance polarizers," *Opt. Exp.*, **14** 2323 (2006).

82. Z.Y. Yang and Y.F. Liu, "Broadband nanowire-grid polarizers in ultraviolet-visible-near-infrared regions," *Opt. Exp.*, **15** 9510 (2007).

83. J.J. Wang, X. Liu, P. Sciortine, and X. Deng, "High-performance, large area, deep ultraviolet to infrared polarizers based on 40 nm line/78 nm space nanowire grids," *Appl. Phys., Lett.*, **90** 61104 (2007).

84. C.-C. Liu, E. Han, M.S. Onses, C.J. Thode, S. Ji, P. Gopalan, and P.F. Nealey, "Fabrication of Lithographically Defined Chemically Patterned Polymer Brushes and Mats," *Macromolecules*, **44** 1876-1885 (2011).

85. S.O. Kim, H.H. Solak, M.P. Stoykovich, N.J. Ferrier, J.J. de Pablo, and P.F. Nealey, "Epitaxial self-assembly of block copolymers on lithographically defined nanopatterned substrates," *Nature*, **424**[6947] 411-414 (2003).

86. S. Xiao, X. Yang, S. Park, D. Weller, and T.P. Russell, "A Novel Approach to Addressable 4 Teradot/in^2 Patterned Media," *Adv. Mater.*, **21**[24] 2516-2519 (2009).

87. M.P. Stoykovich, M. Müller, S.O. Kim, H.H. Solak, E.W. Edwards, J.J de Pablo, and P.F. Nealey, "Directed assembly of block copolymer blends into nonregular device-oriented structures," *Science* **308**[5727] 1442-1446 (2005).

88. S. Ji, C.-C. Liu, G. Liu, and P.F. Nealey, "Molecular Transfer Printing Using Block Copolymers," *ACS Nano*, **4**[2] 599-609 (2009).

89. G. Liu, C.S. Thomas, G.S. Craig, and P.F. Nealey, "Integration of Density Multiplication in the Formation of Device-Oriented Structures by Directed Assembly of Block Copolymer–Homopolymer Blends," *Adv. Funct. Mater.*, **20**[8] 1251-1257 (2010).

90. E. Han, K.O. Stuen, Y.-H. La, P.F. Nealey, and P. Gopalan, "Effect of composition of substrate-modifying random copolymers on the orientation of symmetric and asymmetric diblock copolymer domains," *Macromolecules*, **41**[23] 9090-9097 (2008).

91. H.C. Kim, S.M. Park, and W.D. Hinsberg, "Block Copolymer Based Nanostructures: Materials, Processes, and Applications to Electronics," *Chem. Rev.*, **110** 146-177 (2010).

92. J.P. Bearinger, G. Stone, A.L. Hiddessen, L.C. Dugan, L. Wu, P. Hailey, J.W. Conway, T. Kuenzler, L. Feller, S. Cerritelli, and J.A. Hubbell, "Photocatalytic Lithography of Polypropylene sulfide) Block Copolymers: Toward High-Throughput Nanolithography for Biomolecular Arraying Applications," *Langmuir*, **25** 1238-1244 (2009).

93. L.W. Chang, M.A. Caldwell, and H.S.P. Wong, "Diblock Copolymer Directed Self-Assembly for CMOS Device Fabrication," *Proc. of SPIE*, **6921** 69212M (2008).

94. J.Y. Cheng, D.P. Sanders, H.C. Kim, L.K. Sundberg, "Integration of Polymer Self-Assembly for Lithographic Application," *Proc. of SPIE*, **6921** 692127 (2008).

DISTRIBUTION

1	MS0359	D. Chavez, LDRD Office	1911
1	MS0899	Technical Library	9536 (electronic copy)
1	MS1082	D. Bruce Burckel	1727
1	MS1411	Geoff L. Brennecka	1816
1	MS9110	C.-Y. Peter Yang	8229
1	MS9154	Elaine L. Yang	8242
1	MS9406	Charles A. Steinhaus	8656


Sandia National Laboratories